Lithos 368–369 (2020) 105589

Contents lists available at ScienceDirect

Lithos

journal homepage: www.elsevier.com/locate/lithos

Research Article

Origin of oceanic ferrodiorites by injection of nelsonitic melts in gabbros at the Vema Lithospheric Section, Mid Atlantic Ridge

Daniele Brunelli [a,b,*], Alessio Sanfilippo [c], Enrico Bonatti [b,d], Sergei Skolotnev [e], Javier Escartin [f], Marco Ligi [b], Giorgia Ballabio [a], Anna Cipriani [a,d]

[a] Dipartimento di Scienze Chimiche e Geologiche, Università di Modena e Reggio Emilia, Modena, Italy
[b] Istituto di Scienze Marine, ISMAR-CNR, Bologna, Italy
[c] Dipartimento di Scienze della Terra e dell'Ambiente, Università degli Studi di Pavia, Pavia, Italy
[d] Lamont-Doherty Earth Observatory, Columbia University, NY, USA
[e] Geological Institute, Russian Academy of Sciences, Moscow 119017, Russia
[f] Laboratoire de Géologie, UMR 8538, Ecole Normale Supérieure, PSL Research University, CNRS, Paris, France

ARTICLE INFO

Article history:
Received 30 June 2019
Received in revised form 11 May 2020
Accepted 20 May 2020
Available online 28 May 2020

Keywords:
Oceanic lower crust
Gabbro
Oxide gabbro
Axial magma chamber
Nelsonite
Vema fracture zone

ABSTRACT

Oxide gabbros are a minor but diffuse component of the lower oceanic crust. Their presence poses questions on lower crust exhumation processes and magma differentiation at mid ocean ridges because they are systematically associated with shear zones and are hardly explained by classical fractionation and melt migration models. Here, we report on a study of lower-crust gabbros recovered from the Vema Lithospheric Section at 11°N along the Mid Atlantic Ridge, where oxide gabbros are abnormally abundant relative to ridge centred magmatic intrusives and where we found a peculiar lithological occurrence represented by deformed diorites extremely enriched in Fe-Ti-oxides and apatites. Their complex genetic history reveals a hybrid nature consistent with derivation from high pressure injections of Fe-Ti-P saturated nelsonitic melts in a primitive gabbroic groundmass that induced fracturing, de-compaction, mineral resorption and chemical re-equilibration. Melt injections may occur after intense ductile shearing at the edges of the axial magma chamber following lateral differentiation of primitive melts injected at the centre of the ridge axis segment. We propose a regime of lateral, instead of vertical, melt differentiation along the ridge axis and a possible role for melt immiscibility in the formation of Fe-Ti-P melt pockets in oceanic domains.

© 2020 The Author(s). Published by Elsevier B.V. This is an open access article under the CC BY-NC-ND license (http://creativecommons.org/licenses/by-nc-nd/4.0/).

1. Introduction

Oxide gabbros and ferrodiorites occur commonly in the lower oceanic crust. Despite their relative abundance, a lively debate is still open on their genesis and petrologic significance. Here we develop hypotheses based on an extensive sampling from the Vema Lithospheric Section (VLS) at 11° N along the Mid Atlantic Ridge (Fig. 1), where strongly deformed Fe—Ti diorites are more common than in other oceanic settings. The VLS is the northern wall of the prominent Vema Transverse Ridge (VTR) south of the Vema fracture zone (Fig. 1). This region has been extensively studied over more than 50 years because is one of the rare places on Earth where the oceanic lithosphere is exposed and can be studied over a time interval ranging from the present day back to ~30 Ma (Heezen et al., 1964; Van Andel et al., 1971; Bonatti, 1978, Auzende et al., 1989; Kastens et al., 1998; Bonatti et al., 2003; Brunelli et al., 2006; Cipriani et al., 2009a; Brunelli et al., 2018). The VTR formed 12–10 Ma ago due to rapid uplift of the southern wall of the fracture zone by elastic rebound during a short lived (~1–2 Ma) counter clockwise migration of the Africa-South America plate rotation pole (Bonatti et al., 2003, 2005). The lithosphere was uplifted by 2–4 km over the entire stretch of the transform fault between the eastern and western MAR intersections (*E*-MAR and W-MAR, Fig. 1), exposing a complete section of oceanic crust and part of the upper mantle below the petrological Moho. Direct observations by manned submarine dives in 1988 (Auzende et al., 1989; Cannat et al., 1991) confirmed the prediction of Bonatti (1978), that the VLS exposes a complete section of oceanic lithosphere. Estimated locations of lithological boundaries between the basal residual mantle, intrusive gabbros and extrusive dikes and basalts are reported in Fig. 1.

The accessibility to both the residual mantle and its associated erupted MORBs has played a key role in recognizing the temporal evolution of the petrologic, tectonic and thermal interplay during the formation of the oceanic crust at a single ridge segment, i.e. the *E*-MAR segment (Bonatti et al., 2003; Brunelli et al., 2006, 2018; Cipriani et al.,

* Corresponding author at: Dipartimento di Scienze Chimiche e Geologiche, Università di Modena e Reggio Emilia, Modena, Italy.
E-mail address: daniele.brunelli@unimore.it (D. Brunelli).

https://doi.org/10.1016/j.lithos.2020.105589
0024-4937/© 2020 The Author(s). Published by Elsevier B.V. This is an open access article under the CC BY-NC-ND license (http://creativecommons.org/licenses/by-nc-nd/4.0/).

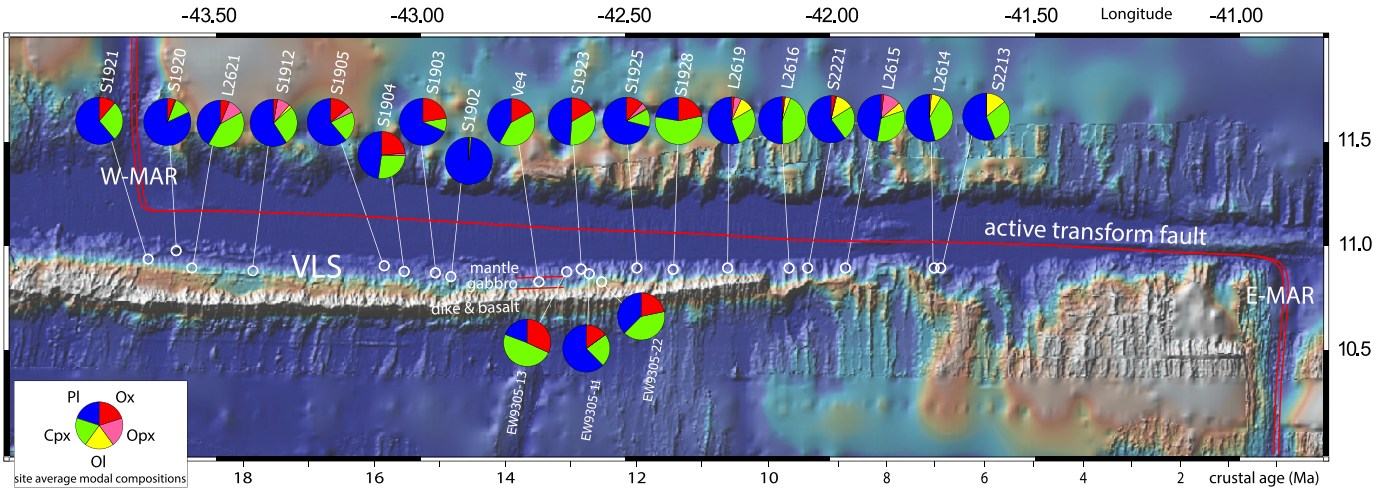

Fig. 1. Shaded relief map of the Vema Transverse Ridge. The pizza plots represent the site average modal composition of the gabbros along the Vema Lithospheric Section. Blue: plagioclase; green: clinopyroxene; red: oxides; yellow: olivine and purple: orthopyroxene. The age of the crust is shown on the lower horizontal axis. Sampled gabbroids range from ca. 7 to 20 Ma in age. The list of dredges and dives is reported in Table 1. Base map is made with GeoMapApp (www.geomapapp.org, Ryan et al., 2009).

2004, 2009a, 2009b). Geophysical evidence revealed that the magmatic productivity of the E-MAR segment (Fig. 1) increased over time, as indicated by a gravity-derived crustal thickening of ~ 1 km during the last 26 Ma (Bonatti et al., 2003; Cipriani et al., 2009a). A petrological and geochemical study of mantle and genetically related extrusive rocks over 26 Ma revealed that thermal diffusion from less to more fertile lithologies during mantle partial melting caused the reduction of the total melt production in the past (Brunelli et al., 2018).

We report here for the first time on petrology and geochemistry of the gabbros from this unique portion of oceanic lithosphere. Lower crustal rocks have been collected during several oceanographic expeditions starting in the late 70s (Table 1). They are dominated by deformed gabbroids (ferrodiorites) showing a marked enrichment in Fe–Ti oxides that range above the normal abundance of these lithologies in oceanic settings. Here we use the term "gabbroids" when referring to the entire association of gabbros and Fe-rich differentiates, or to hybridized rocks, as shown further on. Several studies have suggested a link between Fe–Ti oxide-rich gabbroids and deformation in oceanic sections exhumed at detachment faults (Atkinson, 1977; Dick et al., 1991a, 1991b, 2000; John and Cheadle, 2010; MacLeod et al., 2017; Sanfilippo et al., 2019). However, the origin of these rocks and their correlation with crystal-plastic deformation in large offset transforms remain nearly unconstrained. A wealth of information is provided by deep drilling into the lower oceanic crust, as for instance the Atlantis Bank (South West Indian Ridge, Dick et al., 1991a, 1991b, 2000). This large oceanic core complex exposes deep crustal and lithospheric mantle rocks exhumed in the footwall of an oceanic detachment fault. ODP Holes 735B, 1105A and IODP Hole U1473A at the Atlantis Bank consistently recovered relatively primitive gabbroic sections (olivine gabbro), interspersed by evolved oxide-bearing varieties (Dick et al., 1991a, 1991b, 2000, 2019; MacLeod et al., 2017; Pettigrew et al., 1999). The oxide seams in ODP Hole 735B superimpose the framework of olivine gabbros and gabbros, indicating no consistent relationship with the boundaries of the five upwardly differentiated geochemical cycles (Dick et al., 1991a, 1991b, 2000; Natland and Dick, 2001). This observation has been further supported by MacLeod et al. (2017) who, in line with other recent studies (Koepke et al., 2018; Lissenberg and MacLeod, 2016), interpreted the oxide-gabbros as localized zones of migration, and ultimate emplacement, of late-stage melts not directly related to the chemostratigraphy of the primitive Ol-gabbro background. A detailed microtextural analysis revealed that high-temperature deformation is present equally in both Fe–Ti oxide-bearing and non Fe–Ti oxide-bearing rocks throughout the section (Miranda and John, 2010). This observation follows Bloomer et al. (1991) that proposed oxide minerals precipitation after intense deformation of the host rocks and with absence of subsequent strong deformation.

In this study we show that Fe–Ti rich melts can locally extend to apatite saturation (nelsonites), and that they can be injected during pulses of deformation inducing melt-overpressurization and "hydrofracturing", with the subsequent disruption and partial dissolution of the pre-existing crystal matrix. We use mineral chemistry and textural disequilibrium to constrain injection and melt-induced fracturation, proposing a model where Fe–Ti–P saturated melts can be formed by lateral reactive migration from the centre of the ridge segment toward the ridge-transform intersection.

2. The gabbroic layer at the Vema Lithospheric Section

A vertical section of the gabbroic layer, directly observed and sampled during submersible dives in the 1988 Vemanaute expedition, revealed the presence of a ~ 500 m thick vertical outcrop of Fe–Ti rich gabbros (Auzende et al., 1989; Cannat et al., 1991). The upper contact with the dike complex is primary and undeformed (Cannat et al., 1991) whereas the lower contact with the residual mantle is clearly tectonic and marked by strongly foliated and amphibolitized gabbros and peridotites. This tectonic discontinuity could be related either to primary ridge-building tectonics or to secondary faulting due to the uplift of the transverse ridge, implying that the measured thickness represents a minimum estimate of the vertical extent of the gabbroic layer. Morphologically the gabbro outcrop is marked by a change in the ridge slope, forming a ~ 2 km wide terrace gently dipping northwards. This morphological discontinuity can be followed all along the VLS, suggesting the lateral continuity of the gabbroic layer during this time stretch.

Gabbros were sampled at 21 sites (Fig. 1, Table 1) along the VLS during several expeditions (Auzende et al., 1989, 1990; Cipriani et al., 2009a; Fabretti et al., 1998). Crustal ages at each dredge station are estimated from a flowline based on Africa-South America Euler vectors of Shaw and Cande (1990) adopting the geomagnetic time scale of Cande and Kent (1995). They span over a time interval of ~ 13 Ma, ranging from 6.75 Ma at site S2213, to 19.72 Ma at dredge site S1921 (Fig. 1). Crystallization ages in VLS gabbros have been defined based on U/Pb

Table 1
Starting and ending latitude and longitude, depth interval and rock recovery for the dredge sites.

Dredge	Recovered rocks	Start Lat.	End Lat.	Start Long.	End Long.	Depth interval (m)
Nautile dive						
VE4	Amphibolite, peridotite, gabbro	10°42.9' N	10°40.3' N	42°39.4' W	42°39.2' W	5141–3896
R.V. M. Ewing, cruise EW9305						
EW9305-D11	Peridotite, gabbro, semiconsolidated calcareous ooze, breccia	10°42.5' N	10°42.3' N	42°36.3' W	42°36.3' W	4950–4750
EW9305-D13	Peridotite, gabbro, breccia	10°42.3' N	10°41.7' N	42°38.3' W	42°38.4' W	5050–4700
EW9305-D22	Peridotite, gabbro, dolerite, basalt and limestone,	10°40.6' N	10°40.5' N	42°33.3' W	42°33.3' W	3600–3550
R.V. A.N. Strakhov, cruise S19						
S1902	Peridotite 80%, dunite 1%, gabbro 18%, dolerite 1%	10°42.3' N	10°40.3' N	42°55.1' W	42°55.1' W	4800–3700
S1903	Peridotite 90%, dunite 1%, gabbro 10%, breccia 9%	10°42.4' N	10°41.3' N	42°57.5' W	42°57.2' W	4950–4260
S1904	Peridotite 34%, dunite 1%, gabbro 60% breccia 5%	10°42.6' N	10°41.5' N	43°02.0' W	43°01.7' W	4900–4500
S1905	Gabbro 50%, peridotite 45% basalt/dolerite 5%	10°43.1' N	10°42.6' N	43°04.8' W	43°04.7' W	5050–4750
S1912	Myl/porph peridotite 90%, breccia 5%, gabbro 5%, limestone <1%	10°42.7' N	10°41.6' N	43°24.1' W	43°23.4' W	4500–3700
S1920	Dolerite and basalt 80%, breccia 13%, myl/porph, peridotite 5%, gabbro 2%	10°45.4' N	10°44.7' N	43°34.6' W	43°35.1' W	5000–4550
S1921	Gabbro 100%	10°44.5' N	10°43.2' N	43°38.7' W	43°39.1' W	4850–4000
S1923	Porphyroclastic peridotite 70%, gabbro 20%, limestone breccia 10%	10°42.2' N	10°41.2' N	42°34.5' W	42°35.7' W	5200–4000
S1925	Porphyroclastic peridotite 80%, gabbro 14%,, breccia 4%, ophicalcite 1%, limestone 1%	10°42.6' N	10°42.5' N	42°28.6' W	42°27.8' W	5150–4850
S1928	Porphyroclastic peridotite 95%, gabbro 2%, dolerite 2%, breccia 1%	10°42.8' N	10°41.9' N	42°23.0' W	42°22.9' W	5120–4530
R.V. A.N. Strakhov, cruise S22						
S2213	Gabbro 80%, breccia 15%, basalt 3%, dolerite 2%	10°42.1' N	10°42.1' N	41°44.2' W	41°44.2' W	5100–5100
S2221	Ultramafic rocks 55%, gabbro 28%, basalt 8%, breccia 7%, dolerite 1%	10°43.0' N	10°42.6' N	42°03.7' W	42°03.3' W	4900–4800
R.V. Logachev, cruise L26						
L2614	Porphyroclastic peridotite 2%,gabbro 98%	10°43.5' N	10°42.7' N	41°45.2' W	41°45.5' W	5198–4672
L2615	Porphyroclastic peridotite 80%, gabbro 20%	10°42.9' N	10°42.2' N	41°58.0' W	41°58.0' W	5127–4569
L2616	Peridotite 5%, gabbro 80%, basalt/dolerite 15%	10°43.1' N	10°42.3' N	42°06.2' W	42°06.2' W	5160–4603
L2619	Gabbros 70%, dolerites/basalts 30%	10°42.6' N	10°41.7' N	42°15.1' W	42°14.9' W	5111–4550
L2621	Myl/porph peridotite 15%, gabbro 70%, dolerite 15%	10°45.1' N	10°44.3' N	43°32.6' W	43°33.2' W	5112–4515

zircon systematics (Kostitsyn et al., 2018; Lissenberg et al., 2009; Rioux et al., 2015); for each single intrusion they span from 90 up to 250 ka. These time-intervals provide evidence for the protracted growth of zircons during solidification of each single gabbroic pluton (Lissenberg et al., 2009) and a regular magma delivery over the last 18 Ma (Kostitsyn et al., 2018) resulting in a good correspondence between the magmatic ages and those predicted by plate motion models (Shaw and Cande, 1990).

The constancy and lateral continuity of the magmatic and tectonic accretionary style over this long time interval allow correlations among the Vema gabbros and with other oceanic occurrences. Analyses and inspection of both directional gradient and slope maps of the area provide constraints on the history and mode of accretion of the *E*–MAR segment (supplementary Fig. 1). The bathymetry reveals a clear oceanic fabric, dominated by ridge-parallel abyssal hills, extending up to the Vema transverse ridge along all its length. These abyssal hills have been bent upwards later than their formation by tectonic uplift (supplementary Fig. 1). We did not observe any transform- or spreading-parallel corrugations or smooth surfaces common at oceanic detachment faults. Hence, we infer that the VLS corresponds to an oceanic lithosphere accreted symmetrically at the E–MAR segment, with a relatively high magma supply precluding asymmetric accretion and the formation of oceanic core complexes.

3. Methods

Rock sampling along the VLS has been carried out primarily by conventional dredging during several expeditions; therefore samples are not oriented, and a single dredge haul may contain mixed lithologies representative of the entire lithospheric section above the dredge track. Samples labelled Ve- have instead been collected in situ by manned submersible dives during the Vemanaute expedition (Auzende et al., 1989), hence their geological context is known.

Modal mineralogy was determined on high definition images of thin sections and contextual microscopy optical check using the image analysis toolbox JMicroVision (Roduit, 2019). We used a recursive grid counting for at least 1500 points per each thin section. Point counting is stopped based on the cumulative evolution plot when the fluctuation of the measured phases is $< \pm 0.5\%$. Coarse grain size rocks average two regular thin section surfaces. In order to define the primary high–T mineralogy amphibole pseudomorphs on Cpx are attributed to Cpx; serpentine $\pm$ magnetite or iron oxides are attributed to Ol. Point counting was only performed on rocks with evident high–T paragenesis, hence, pervasively amphibolitized or weathered rocks were not included in the modal analysis.

Backscatter SEM images were obtained by recombining the single major element density channels collected at the Centro Interdipartimentale Grandi Strumenti (CIGS, Università di Modena e Reggio Emilia, Italy) on C–coated thin sections in backscattered and secondary electron modes using an environmental scanning electron microscope Quanta-200 (Fei Company–Oxford Instruments) at 12–20 kV accelerating voltage.

Major-element mineral compositions were analysed in two labs by electron probe microanalysis (EPMA): a first batch was analysed with a JEOL JXA–8800 Superprobe system at Kanazawa University, using an accelerating voltage of 15 kV and beam current of 20 nA, using a 3-μm beam. JEOL software using ZAF corrections was employed, analytical details are reported in Sanfilippo et al. (2015). A second batch was analysed using the automated CAMECA-CAMEBAX electron microprobe of the CAMPARIS micro-analysis centre (University of Paris 6). A 5 μm beam size was used for all minerals, with an accelerating voltage of 15 kV and a beam current intensity of 40 nA. Elemental maps were obtained by recombining single major element density channels produced on 256 × 256 and 512 × 512 acquisition grids at 15 keV – 45 nA with grid steps of 7 and 5 μm respectively. A set of natural and synthetic mineral standards were used for all minerals following standard procedures defined in Seyler and Brunelli (2018). Inter-calibration between the two analytical sessions has been achieved by deriving relative correction factors using two samples as internal standard (S1925–02 and EW9305–11D). Relative corrections on the raw data are applied to reduce the difference in concentration below the 1σ observed sample variability (< 10% for Si, Al, Fe, Mg, Ca and < 5% for Ti, Cr, Mn, Na, K, Ni).

Mineral abbreviations follow IUGS recommendation: olivine Ol, plagioclase Pl, Orthopyroxene Opx, Clinopyroxene Cpx, Amphibole Am, Apatite Ap, ilmenite Ilm, magnetite Mag. For general terms: pyroxene Px, oxide Ox.

4. Modal composition and texture of the VLS gabbroids

Dredged rocks represent a stochastic sampling of the gabbroic layer overlying the basal mantle section. In hand-specimen, they consist of sub-rounded rubbles of relatively small dimensions (<15 cm in diameter), with some rare occurrences larger than 20 cm.

The gabbros from the VLS vary from troctolite to oxide-gabbro (Skolotnev, 2003) covering the entire range of oceanic gabbroic lithologies. However, primitive lithologies, as troctolite or Ol-rich gabbros, are rare among the collected rocks, and limited to sites from the youngest sectors of the VLS, and those in normal crust formed in the last 10 Ma east of the VTR (sites to the east of dredge L2619, Fig. 1). In samples dredged from the VLS, olivine occurs as a minor phase (<3 vol%), or is totally absent (Table 2, Fig. 1).

A simplified classification is adopted in the plots to highlight lithological differences based on modal distribution. We defined as gabbro all rocks where olivine, orthopyroxene and oxides are each less than 5%. Then, olivine gabbro for Ol > 5% and Ox < 5%; oxide gabbro when Ox > 5% and gabbronorite when Opx > 5%.

Overall, the modal distribution of VLS gabbros tends toward evolved lithologies, being on average more evolved than sites representative of axial- or core complex-related gabbroic sequences (Fig. 2). For comparison we show the proportions of different lithologies for Hole U1309D in the Atlantis Massif at 30°N on the MAR (Blackman et al., 2006), and Hole 1473A from Atlantis Bank at 57°E on the SW Indian Ridge (MacLeod et al., 2017). Compared to the VLS gabbros, the lithological distribution of gabbroic rocks in these two long sections is generally richer in primitive lithologies, i.e. troctolite and primitive olivine gabbro, and poorer in oxide-bearing rocks (Fig. 2). Specifically, the VLS gabbros with more than 5 vol% oxides represent ≈56% of the total recovery, even though not uniformly distributed along the temporal section (Tables 1 and 2). We note, however, that high Fe–Ti oxides bearing lithologies characterize also the lower crust exposed along the Atlantis II transform, interpreted by Dick and co–authors (2019) to represent the peripheral portion of the gabbroic pluton drilled at IODP Hole U1473A.

The oxide distribution in VLS lower crustal rocks defines a correlation with other phases different from that of the Atlantis Bank and Atlantis Massif sections, possibly following a trend where modal increase in oxides is associated with a decrease in plagioclase and, by consequence, with an increase in clinopyroxene modal content (Fig. 3). The VLS gabbroids thereby are richer in oxide and clinopyroxene than those from other oceanic gabbroic sites. The oxide-rich gabbroids represent the main constituent of the VLS lower crust.

Several VLD gabbros display intense plastic deformation (38 out of 62 samples studied) commonly with a protomylonitic to mylonitic texture (Table 2). Undeformed cumulates are a relatively minor occurrence; those with ophitic and granular/inequigranular textures have generally medium grainsize (Fig. 4A–C), whereas those showing poikilitic grains of clinopyroxene including plagioclase and olivine have coarse grain size (Fig. 4B, Table 2). These textural relationships are observed regularly in the oceanic lower crust due to progressive melt/rock reaction in crystal mushes (Lissenberg and Dick, 2008). Here we focus on the most deformed lithologies that are markedly enriched in oxides. These rocks show a fine-grained, locally layered, matrix of neoblastic plagioclase and pyroxene surrounding sub-rounded, locally irregular, plagioclase and pyroxene porphyroclasts (Fig. 4D–F). The neoblastic matrix is rather inhomogeneous in grain-size at both the thin section and sample scale. Overall protomylonitic terms prevail (neoblastic matrix<30%) over mylonites (matrix 50–90%). The neoblastic matrix is often disrupted by a discordant sub-millimetric network of veins and fractures rich in Fe—Ti oxide (± apatite) (Fig. 4E-F). Fe–Ti oxides are rarely present as micro-veins or layers concordant to the high-T mylonitic foliation. The oxide seams locally contain apatite enrichment distributed inhomogenously in the rock, concentrated mainly, but not exclusively, in the largest pockets (Fig. 4F). Protomylonitic terms are sometimes overprinted by lower temperature cataclasis (7 samples, see Table 2).

In the Fe–Ti oxide-rich samples, the former intrusive magmatic phases are generally affected by a pervasive substitution at conditions varying from nearly magmatic to low–T hydrothermal alteration and subsequent weathering. The most obvious effect is the formation of amphibole that can be used as a proxy to track processes from infiltration/percolation of late-stage melts to deformation and hydrothermal alteration.

Amphiboles in the VLS gabbros and Fe-diorites can be grouped in four different textural types: 1 to 4 listed below. They show a progressive decrease of P-T, in a retrograde history ranging from purely magmatic to purely metamorphic/hydrothermal conditions.

Type 1 is represented by fine-grained pink/brown amphibole grains, found as interstitial grains or films in poorly deformed samples and locally associated to Fe–Ti oxides (supplementary Figs. 2A, B). Type 2 consists of large reddish/brown amphibole grains often associated to Fe–Ti Ox, Ap and locally Opx (supplementary Figs. 2C and 2D). These amphiboles are often associated to oxide networks partially replacing former Cpx or Pl + Cpx neoblastic assemblages. Type 3 is represented by amphibole porphyroclasts and, locally, neoblasts within the mylonitic samples (supplementary Fig. 2E, F). They appear as pseudomorphs on Cpx (supplementary Fig. 2F) or in neoblastic assemblages with Pl (supplementary Fig. 2E) or as substitutions on Cpx within Ap + Pl neoblastic assemblages. Type 4 consists of dark green amphibole pseudomorphs on pyroxenes and in neoblastic assemblages with low grade metamorphic minerals (Pl ± Chl ± Ep) (supplementary Figs. 2G and 2H). These amphiboles are the main component of those samples defined as "amphibolites" (Honnorez et al., 1984), to indicate a complete substitution of the original pyroxene under hydrous conditions. Texturally type 1 and 2 amphiboles can be related to interactions with variably hydrated melts, while type 3 and 4 can be linked to recrystallization during deformation or static replacement under upper amphibolite to lower greenschist metamorphic conditions.

5. Mineral chemistry

Chemical compositions of the minerals in the VLS gabbros are imaged by co-variation diagrams, such as anorthite (An) content in plagioclase versus Mg# in coexisting clinopyroxene (Fig. 5). VLS gabbroids show two compositional groups: olivine gabbros and oxide-rich diorites. Although the latter are generally defined as Fe-gabbro or flaser gabbro, the An contents lower than 50% classify them as diorites following Streckeisen (1973), Le Maitre et al. (2002) and Mazzucchelli (2016). Compositionally primitive terms are not present in the collected gabbros in agreement with their modal composition.

Ol–gabbros show a strong variability of An content and do not define a linear trend as instead observed in single gabbroic sequences from the Pacific, Indian and Atlantic oceans (Fig. 5). The oxide-rich group contains phases equilibrated to more evolved conditions. Plagioclase is mainly andesine with An% ranging 25–50, Cpx Mg# 55–77, and Ol, when present, ranges from Fo 36 in the more evolved assemblages to Fo 62 in the less evolved (Supplementary Data Table 3). Olivine is generally partly dissolved and replaced by Fe—Ti Ox-apatite assemblages. These relic olivines are significantly drawn toward the fayalitic end member relative to the equilibrium olivine expected in a gabbroic association. These olivines have extremely variable but lower NiO content than those in the Ol–gabbros (Fig. 5B, Supplementary Data Table 3).

Table 2
Modal composition, texture and grainsize of the Vema gabbroids.

Sample	Pl	Cpx	Ol	Opx	Ox	Texture	Grainsize (for mylonites it refers to porphyrocalsts)
EW9305-11D1	48.86	34.48	0	0	16.65	Protomylonitic	Medium
EW9305-13D4	19.29	48.92	0	0	31.79	Protomylonitic	Medium
EW9305-22D8	37.54	40.73	0	0	21.73	Mylonitic	Medium
S1902–04	98.36	1.31	0	0	0.33	Protomylonitic	Medium
S1903–02	68.36	9.19	0	0	22.45	Mylonitic	Medium
S1904-01A	67.62	16.34	0	0.3	15.74	Mylonitic	Medium
S1904–06	27.32	30.84	0	0	41.83	Mylonitic	Medium/Coarse
S1904–10	69.48	8.89	0	0	21.63	Protomylonitic/Cataclastic	Medium
S1904–17	47.13	37.92	0	0	14.95	Protomylonitic	Medium
S1904–28	27.37	40.7	0	7.6	24.33	Mylonitic	Fine/Medium
S1905-01A	68.2	8.49	0	16.48	6.83	Protomylonitic	Medium
S1905–19	36.34	45.34	0	0	18.32	Protomylonitic	Coarse
S1905–53	93.26	0.63	0	0	6.11	Protomylonitic	Coarse
S1905–105	47.06	28.84	0	0	24.1	Mylonitic	Medium
S1912–01	59.13	27.27	2.05	8.94	2.61	Ophitic/Poikilitic	Medium
S1920–64	60.77	35.75	0	2.4	1.07	Ophitic	Medium
S1920–95	89.01	4.27	0	0	6.72	Protomylonitic	Coarse
S1921–01	27.52	50.25	0	0	22.23	Protomylonitic/Cataclastic	Medium/Coarse
S1921–03	94.74	4.91	0	0	0.35	Cataclastic	Medium
S1923–01A	34.61	29.6	0	0	35.79	Protomylonitic	Medium/Coarse
S1923–01B	58.42	26.53	0	0	15.05	Protomylonitic	Medium/Coarse
S1923–03	58.16	18.99	0	0	22.85	Mylonitic	Medium
S1923–09	31.64	43.68	0	0	24.67	Protomylonitic	Medium
S1923–12	66.48	21.98	0	0	11.54	Protomylonitic	Medium/Coarse
S1923–16	56.2	31.01	0	0.38	12.41	Mylonitic	Medium
S1923–20	94.55	3.64	0	0	1.82	Mylonitic/Cataclastic	Medium
S1923–21	70.61	18.04	0	0	11.35	Protomylonitic	Medium/Coarse
S1923–24	80.33	11.95	0	0	7.73	Protomylonitic	Medium/Coarse
S1923–88	73.4	20.52	0	0	6.08	Protomylonitic/Cataclastic	Medium
S1925–01A	77.19	0.7	2.34	12.36	7.41	Mylonitic	Medium
S1925–01C	86.83	4.91	2.27	4.48	1.51	Mylonitic	Medium
S1925–02A	55.82	26.68	0	5.03	12.46	Mylonitic	Medium
S1925–02B	75.72	5.85	0	4.26	14.18	Mylonitic/Cataclastic	Medium
S1925–03	51.28	22.76	0	0	25.96	Mylonitic	Medium
S1925–8A	72.96	14.35	0.33	4.32	8.04	Mylonitic	Medium
S1925–8B	72.83	11.01	0	3	13.16	Mylonitic	Medium
S1925–14	75.63	11.63	0	0.71	12.02	Mylonitic	Medium
S1928–04	22.31	56.04	0	0	21.65	Protomylonitic	Medium/Coarse
Ve4–9H	66.58	28.97	0	0	4.45	Protomylonitic	Medium/Coarse
Ve4–9B	17.22	52.82	0	0	29.96	Protomylonitic	Medium/Coarse
L2614–01	57.43	32.38	7.33	2.04	0.81	Ophitic	Medium
L2614–02	54.64	43.85	1.28	0	0.23	Ophitic/Poikilitic	Medium
L2614–05B	53.99	40.05	3.68	2.03	0.25	Ophitic	Medium
L2614–08	57.19	34.7	6.23	1.2	0.68	Equigranular	Medium
L2614–09	47.75	37.27	14.42	0.37	0.19	Equigranular	Medium
L2614–33	52.64	38.1	8.89	0	0.36	Granular	Medium
L2615–03	47.27	28.51	10.37	13.48	0.37	Inequigranular	Medium/Coarse
L2615–04	47.88	33.96	2.56	14.88	0.72	Inequigranular	Medium
L2615–17	46.92	36.19	4.62	8.08	4.19	Ophitic	Medium
L2616–07	44.62	52.67	0	2.33	0.39	Ophitic	Medium
L2616–08	60.13	37.78	1.83	0	0.26	Poikilitic	Coarse
L2616–09	41.67	52.35	5.39	0	0.59	Ophitic/Poikilitic	Medium
L2616–12	55.4	32.22	7.62	0.63	4.13	Ophitic/Poikilitic	Medium/Coarse
L2619–03	55.39	28.08	9.77	5.01	1.75	Ophitic/Poikilitic	Medium
L2621–03	41.56	41.56	0	10.78	6.11	Inequigranular	Medium
S2213–01A	49.52	32.17	18.31	0	0	Inequigranular	Medium
S2213–16	59.16	33.15	7.55	0	0.14	Ophitic/Poikilitic	Medium
S2213–17	63.54	10.07	25.69	0	0.69	Ophitic	Medium
S2213–52	51.81	44.56	3.37	0	0.26	Equigranular	Medium
S2221–54	56.66	33.25	9.09	0.12	0.87	Ophitic	Medium
S2221–60	71.72	0	28.28	0	0	Equigranular	Fine/Medium
S2221–62	51.79	37.95	0	2.15	8.11	Inequigranular	Medium/Coarse

Amphiboles show a clear compositional dependence on textural position, as defined in the previous paragraph. Amphibole types 1 and 2 have pargasitic, and minor edenitic composition (Fig. 5B), while type 3 and 4 plot mainly in the hornblende compositional field. With respect to amphiboles in ultramafic mylonites and peridotites recovered in the associated VLS mantle section (Cipriani et al., 2009b), those in gabbros are more enriched in Ti while partially overlap the alkali composition in the higher and lower T terms.

6. Discussion

6.1. Oxide diorites: petrographic evidence for the presence of P, Ti, Fe -rich melts intruding pre-existing gabbroic mushes

Fe–Ti Oxide (±Ap) mineral enrichments in VLS gabbros are in general arranged in anastomosing layers and interstitial schieleren patches discordant from the mylonitic foliation (Figs. 4D–F) and along highly

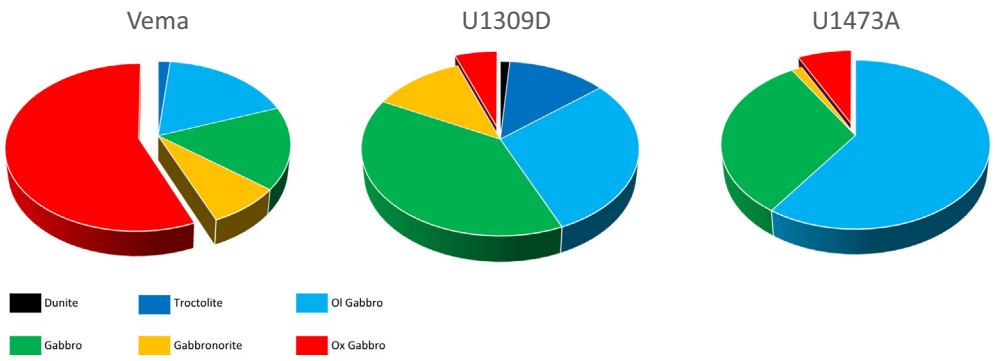

Fig. 2. Lithological distribution of Vema lower crustal rocks compared with two reference gabbroic complexes recovered at axial domain core complexes: drilling sites U1309D and U1473A, from the Atlantis Massif (MAR) and the Atlantis II Bank (SWIR) respectively. Oxide gabbros (red sector) are shifted from the pizza plot to highlight the anomalous abundance of oxide bearing gabbroids along the VLS.

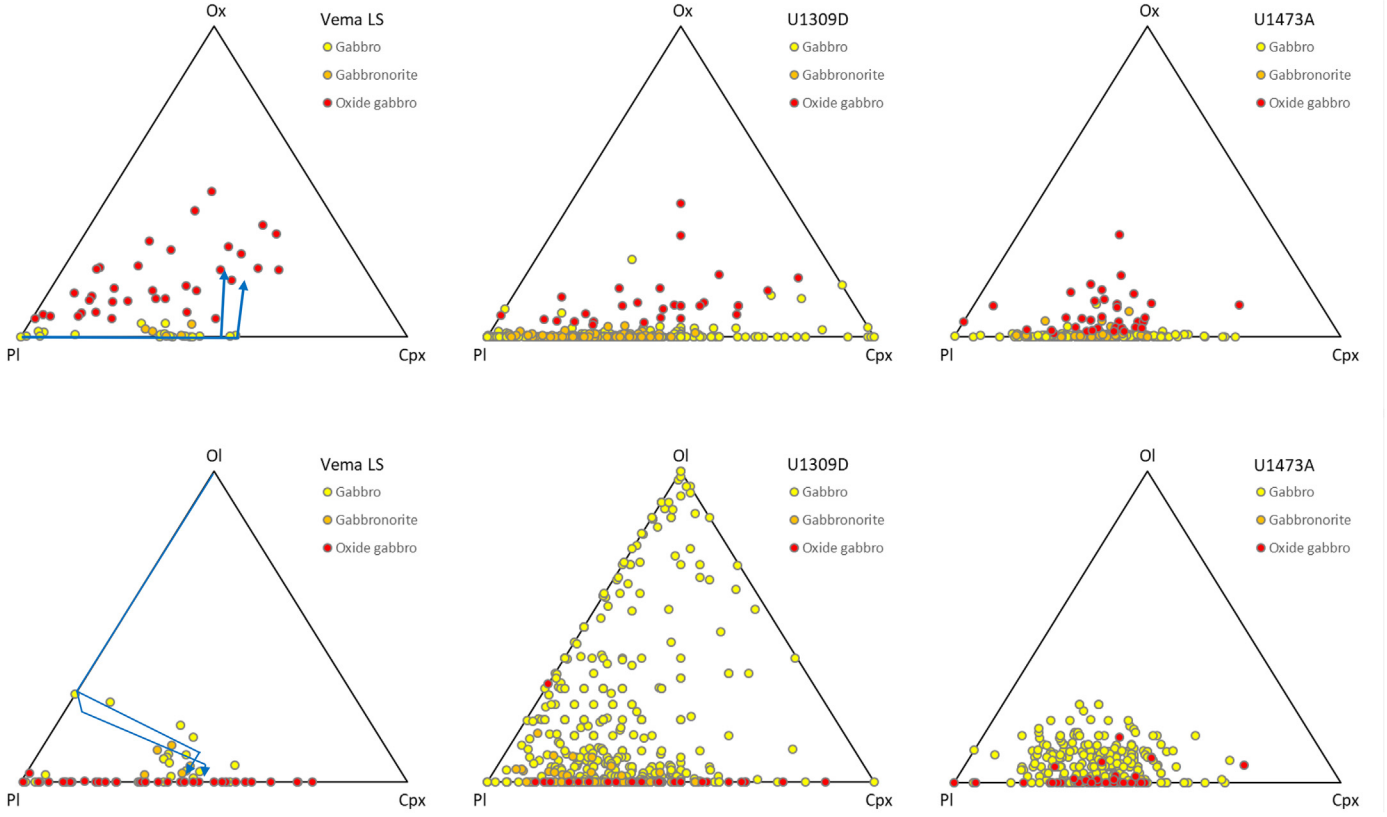

Fig. 3. Modal distribution of the lower crustal rocks from the VLS compared to gabbros from holes U1309D and U1473A (Atlantis Massif, MAR, and the Atlantis II Bank, SWIR, respectively). Blue lines show simplified reference paths for fractional crystallization of a primitive tholeiitic melt calculated at 1 and 3 kbar using Petrolog 3 (Danyushevsky and Plechov, 2011).

deformed layers of variably amphibolitized gabbroic assemblages (Honnorez et al., 1984). These petrographic characteristics are common among other abyssal oxide-gabbro occurrences, mainly represented by strongly sheared rocks with mylonitic bands and a bimodal compositional layering (e.g. Dick et al., 2000; Koepke et al., 2018; MacLeod et al., 2017).

Two main textural relationships can be recognized in the VLS oxide gabbros; they may mark two distinct, although contiguous, petrological events.

1) A first and common textural feature is shown in Fig. 6A-B. These rocks contain sub-millimetric to mm-thick intercalations of Ox-rich and Ox-free layers. Fine-grained apatite forms irregular bands within the oxide-rich layers (Fig. 6C) extending locally into the matrix cracks. Irregular, corroded pyroxene porphyroclasts are mantled by fine-grained assemblages of Mag + Ilm + Ap (Fig. 6D). Locally these rocks display also textural characters that document a gradual transition to brittle deformation. For instance, the apatite-rich seams in Fig. 6C are discordant relative to the direction of the main oxide vein. The plagioclase grains at the tip of these splines are surrounded by Mag-Ilm branchy crystals and show irregular, curved grain boundaries indicative of partial dissolution. In addition, large oxide-rich layers present a gradational grain distribution. For instance in Fig. 6E, plagioclase and apatite grains along with large clasts of the microcrystalline plagioclase matrix are abundant in the lower part of the vein. Small euhedral apatite grains are accumulated together with subhedral to anhedral plagioclase grains. Clasts of Pl (± Cpx) of the mylonitized groundmass clearly

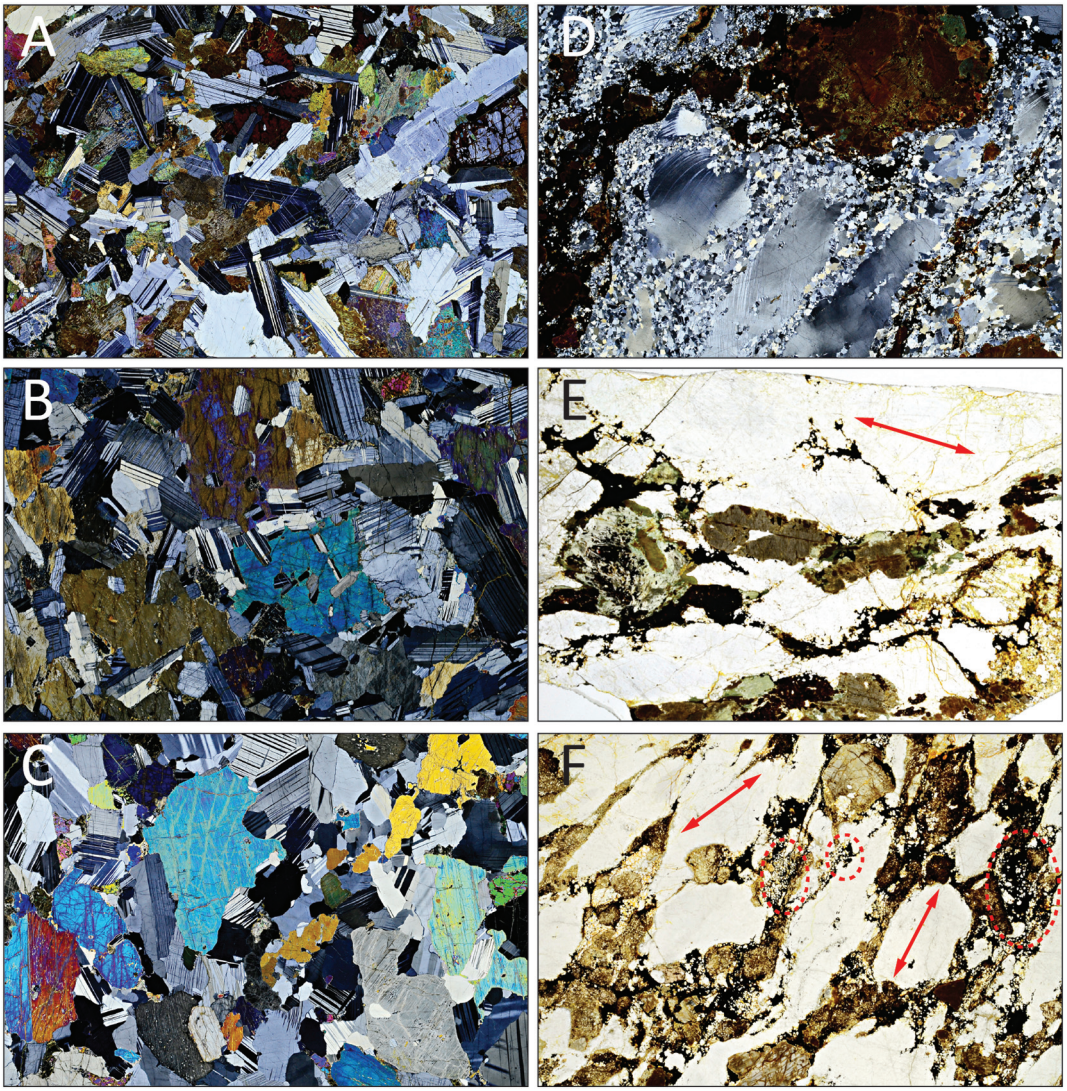

Fig. 4. Micro-images of significant textural occurrences in the VLS gabbros. The base of the picture measures 30 mm long for all insets. Images A-D are crossed nicols; *E*-F parallel light. A: Ophitic texture in gabbro S1920–64. B: Ophitic/poikilitic texture in gabbro L2614–02. C: Inequigranular texture in gabbronorite sample L2615–04. D: Discordant oxide patches cutting the protomylonitic texture in oxide gabbro S1923–01 (see also details in Fig. 6A). E: Anastomosed oxide network discordant with the direction of the protomylonitic foliation (red arrow) in sample S1923–24. F: Brittle anastomosed oxide network dissecting the protomylonitic foliation in sample S1925–07. The orientation of the protomylonitic foliation is shown by the red arrows. Dotted red ellipses show the location of some major enrichment of subhedral apatite grains in an oxide matrix.

snatched out from the matrix are frequent (Fig. 5E). A gradual variation in grainsize distribution is evident, marked by levels of smaller grains close to the lower contact and larger grains toward the centre of the oxide layer. The upper part of the layer is instead enriched in pyroxene clasts. Since all samples described here are not oriented, relative directions cannot be related to any regional deformation structure and stress regime.

2) A second microtextural occurrence is represented by oxide seams and patches showing a lineation systematically discordant with respect to that of the groundmass (Figs. 4E-F and 7). Although locally subconcordant with the mylonitic foliation, the oxide patches appear to fill cracks in a partly disrupted groundmass with evidence of local dissolution and cataclastic deformation of a former mylonitic gabbroic matrix (Fig. 7). A large number of randomly oriented interstitial apophyses depart from the oxide patches surrounding plagioclase crystals and infiltrating into the mylonitic matrix (Fig. 7B). Plagioclase grains are progressively disrupted and isolated from their matrix (Fig. 7A), and locally rounded (Fig. 7B); the most isolated grains inside the oxide-rich patches are more rounded than those close to the groundmass. Small portions of the groundmass are present as isolated clasts inside the oxide patches. The mylonitic fabric of these isolated clusters is frequently rotated with respect to the non-disrupted groundmass. These observations imply some degree of decompaction of the deformed gabbroids.

These petrographic relationships are evident in samples where oxides are associated to a cataclastic texture, as for instance in samples S1923–01; S1923–24 and S1925–07 in Figs. 4D-F, and in sample S1925–02 in Fig. 8. The latter shows fracturing-generated cm-sized clasts of a fine-grained gabbroic mylonite (Figs. 8A-C). Although cracks preferentially follow the high-T foliation of the pyroxene porphyroclasts, some small clasts are partially rotated. Alignments of Pl and Cpx neoblasts are also clearly visible in the less deformed areas of the sample. Crack infilling consists of a fine intergrowth of Mag + Ilm and abundant Ap arranged in irregular to elongated clusters (SEM maps in Figs. 8D-G). Both oxide and apatite also fill thin cracks cutting discordantly both the large plagioclase porphyroclasts (Figs. 8D-F) and the

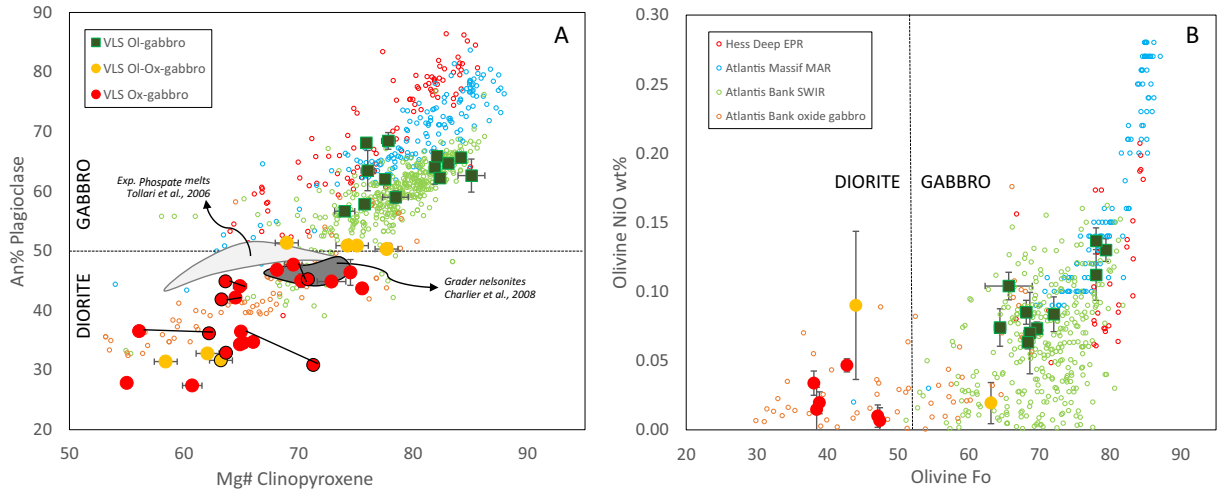

Fig. 5. A: Plagioclase anorthite content vs. clinopyroxene Mg#. Black solid circles highlight rim and neoblast compositions. Large grain cores and rims or associated neoblasts are connected with a solid line. Rocks containing plagioclase with An<50% are defined as diorite (ferrodiorite). The dark grey field shows the composition of nelsonites from the Grader layered intrusion (Charlier et al., 2008); light grey field is the phase composition of experimental charges from Tollari et al., 2006. Background values are from the Atlantis bank (SWIR), Atlantis Massif (MAR) and Hess Deep (EPR) lower crustal rocks (see text for references and discussion). B: NiO versus forsterite contents in olivine of the VLS gabbroids. Background reference values are the same as in the left panel.

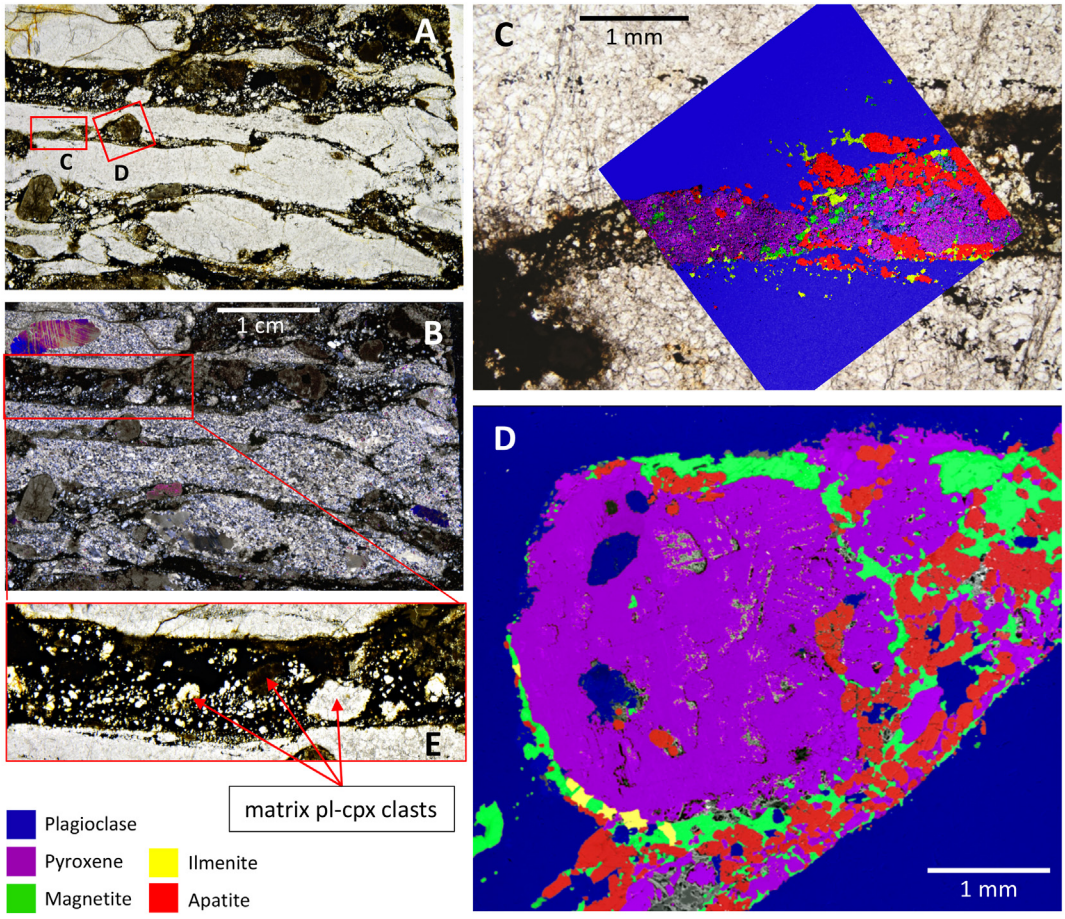

Fig. 6. Example of oxide-rich layering subconcordant with the mylonitic fabric: sample S1925–06. A and B: images of the entire thin section in parallel light (A) and crossed nicols (B). C and D: false colours map after backscatter SEM imaging, see legend for assigned colours; inset C: a stretched pyroxene porphyroclast elongated in the mylonitic foliation is disrupted and sealed by seams of subhedral apatite and minor ilmenite and magnetite. Apatite and oxide accumulate along lateral splines deviating from the main mylonitic foliation marked by the plagioclase neoblast lineation. Inset D: large pyroxene porphyroblast mantled by a tiny apatite and oxide aggregate. Pyroxene neoblasts (± Am) are distributed in the layer concordant with the foliation. Inset E: internal grading of the oxide rich layer given by abundant tiny apatites accumulated in the lower part of the layer mixed with large clasts made of parts of the plagioclase and clinopyroxene deformed groundmass.

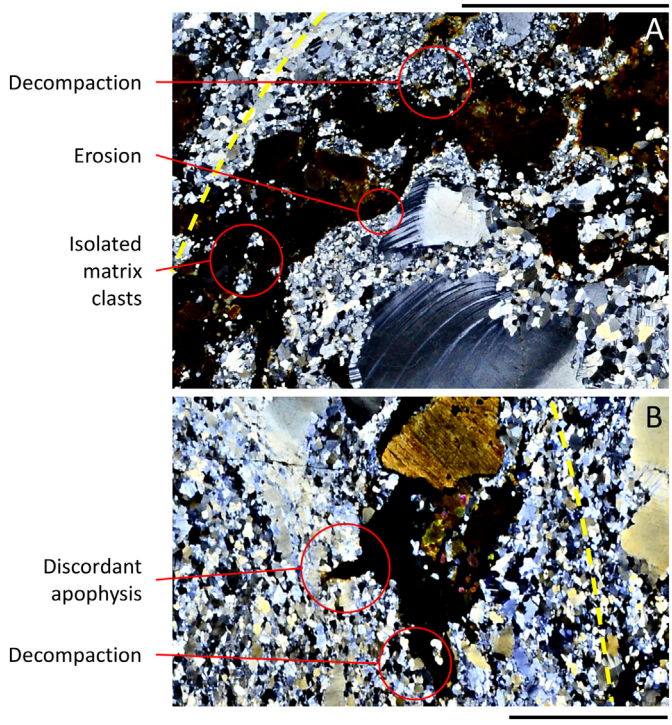

Fig. 7. Details of the oxide patches discordant with the deformation pattern of the mylonitized gabbro. A: Matrix clasts and plagioclase grains are isolated and partially resorbed in sample S1923–01. The progressive isolation of clasts of the groundmass results in a progressive decompaction of the protomylonitic texture (see also Fig. 2D for a larger view of this sample). B: Oxide apophysis clearly cut the mylonitic foliation in sample S1904–04. A yellow dashed line shows the direction of the groundmass foliation. Scale bar is 5 mm.

neoblast aggregates of small plagioclase grains. Small plagioclase and pyroxene grains isolated in the oxide patch are rounded and smoothed suggesting partial resorption (Figs. 8E and G).

6.2. A hybrid origin for the ferrodiorites

Expected compositional trends for fractional crystallization of a primitive MORB at 1 and 3 kbar (Petrolog 3, Danyushevsky and Plechov, 2011) show that although fractional crystallization of Ol, Pl and Cpx can potentially account for the transition from olivine gabbro to gabbronorite, the same process cannot reproduce the trends defined by the oxide-bearing gabbros (Fig. 3).

In the Pl–An% vs. Cpx–Mg# compositional space, the Pacific, Indian and Atlantic Ocean reference populations define three distinct trends shifted at different An contents. This distinction depends primarily on the Na content of the parental melt of each gabbroic population, in turn related to the average mantle degree of melting and, consequently, to spreading rate. The VLS lower crust does not appear to follow any of these trends, as the most primitive Ol-gabbros are highly scattered (green square symbols in Fig. 5). This possibly reflects the nature of the VLS lower crust that contains polygenic, multiple intrusions, scattered over a long time interval (~ 13 Ma). During this time the degree of melting of the residual mantle shows a high frequency variability (3–4 Ma cycles) superposed to a long-lasting steady increasing trend (Bonatti et al., 2003; Brunelli et al., 2006; Cipriani et al., 2009a). An increase of the total amount of melt should result in an increase of the gabbro differentiation, due to the enhanced reactive vertical and lateral differentiation. Instead, primitive Ol-rich lithologies are abundant only in the youngest part of the VLS (Fig. 1).

Oxide gabbros show an even stronger variability than Ol-bearing lithologies (Fig. 5) with no systematic core-rim or large grain vs. neoblast correlation (Fig. 5A). The fluctuations of NiO in olivine could result from interactions with percolating melts due to the dependence of Ni partitioning in olivine on melt composition (Matzen et al., 2013; Sanfilippo et al., 2013). Moreover, olivine can form by reaction of orthopyroxene with magnetite as reported in the oxide gabbro L2612–41 by Pertsev et al. (2015). All together the observed compositional variability implies an incomplete re-equilibration between an exotic (oxide-saturated) melt and a pre-existing gabbro thus suggesting a process postdating near-equilibrium differentiation.

This is further supported by microtextural relationships showing that: i) the oxide-rich seams are variably discordant to the high-T foliation of the host mylonites (Figs. 4E-F, Figs. 6-8); ii) they contain abundant clasts of the mylonitic matrix (Figs. 6E and 7); iii) they are associated with subgrain discordant fractures (Figs. 4D-F, 8F), and iv) are likely related to progressive matrix disruption and decompaction (Fig. 7). We interpret these observations as evidence for injection of a Fe–Ti–P saturated melt into the rock either in the late phases or closely after a high-T ductile event affecting the gabbroic layer. The presence of an oxide-rich corona around the sub-rounded pyroxene and subconcordant oxide seams (Fig. 6D) also suggests the oxide-saturated melt injection started during the deformation event. However discordant, cataclastic relationships in the same thin section (Fig. 6E) reveal that the process extended over brittle conditions. Lateral tiny extensions from the main oxide directions can be interpreted as synthetic splines from main fractures (Fig. 6C), which underwent infiltration and local crystallization of highly-differentiated melts as shown in experimental analogous (e.g. Rosenberg and Handy, 2001). A transition to brittle deformation controlled by temperature reduction can be ruled out. Therefore, we suggest that melt overpressure may have induced cataclasis by “hydrofracturing” and decompaction, followed by a relaxation phase when the melt partially dissolves the disrupted matrix and eventually intrudes laterally through grain boundaries (Figs. 6-8). Local apatite accumulation may be due to microscale dynamic effects as pressure-filtering during percolation of a crystal-bearing melt (Figs. 8D-E). These apatites tend to acquire a subhedral habit, particularly in the larger grains. We infer that the distribution of oxides in these rocks was controlled primarily by infiltration of highly differentiated melts at conditions across the ductile/brittle transition.

The lack of chilled margins indicates that the process occurred at high temperatures with a limited temperature contrast between incoming melt and intruded rock, supporting a pressure instead of a temperature driven transition in deformation regimes. Further evidence for high-temperature conditions of the event is provided by the interstitial distribution of oxide-bearing melts that results in local decompaction of the fine grained plagioclase and pyroxene matrix, with isolation and partial dissolution of the single grains (Figs. 6 and 7). The partial resorption is documented by the rounded shape of both small and large grains of plagioclase and pyroxene (Figs. 8D and E).

Additional constraints on the thermal conditions of these processes can be inferred from the equilibration temperatures calculated with the amphibole-plagioclase and magnetite-ilmenite thermometers. Type 1 and 2 amphiboles show the compositional characters of amphiboles crystallized at magmatic conditions having high Ti and Na + K contents at higher Al^{IV} and lower Si contents (Fig. 9, Supplementary Data Table 3). The amount of aluminium in tetrahedral coordination (Al^{IV}) is a reliable temperature proxy (Blundy and Holland, 1990), also considering the restricted pressure range for melt accumulation at MAR conditions (between 1 and 2 kbar). The Al^{IV} variability of Fig. 9 shows a continuous temperature decrease from type 1 to type 4 mineral assemblages. A qualitative temperature sequence can be inferred by the Ti distribution (Ernst and Liu, 1998), as reported in Fig. 9A. It appears that amphiboles associated with oxide-apatite assemblages (types 1–2) formed at temperatures ranging from 700 °C to 950 °C, thus partly overlapping the temperature of amphiboles stable in late-stage

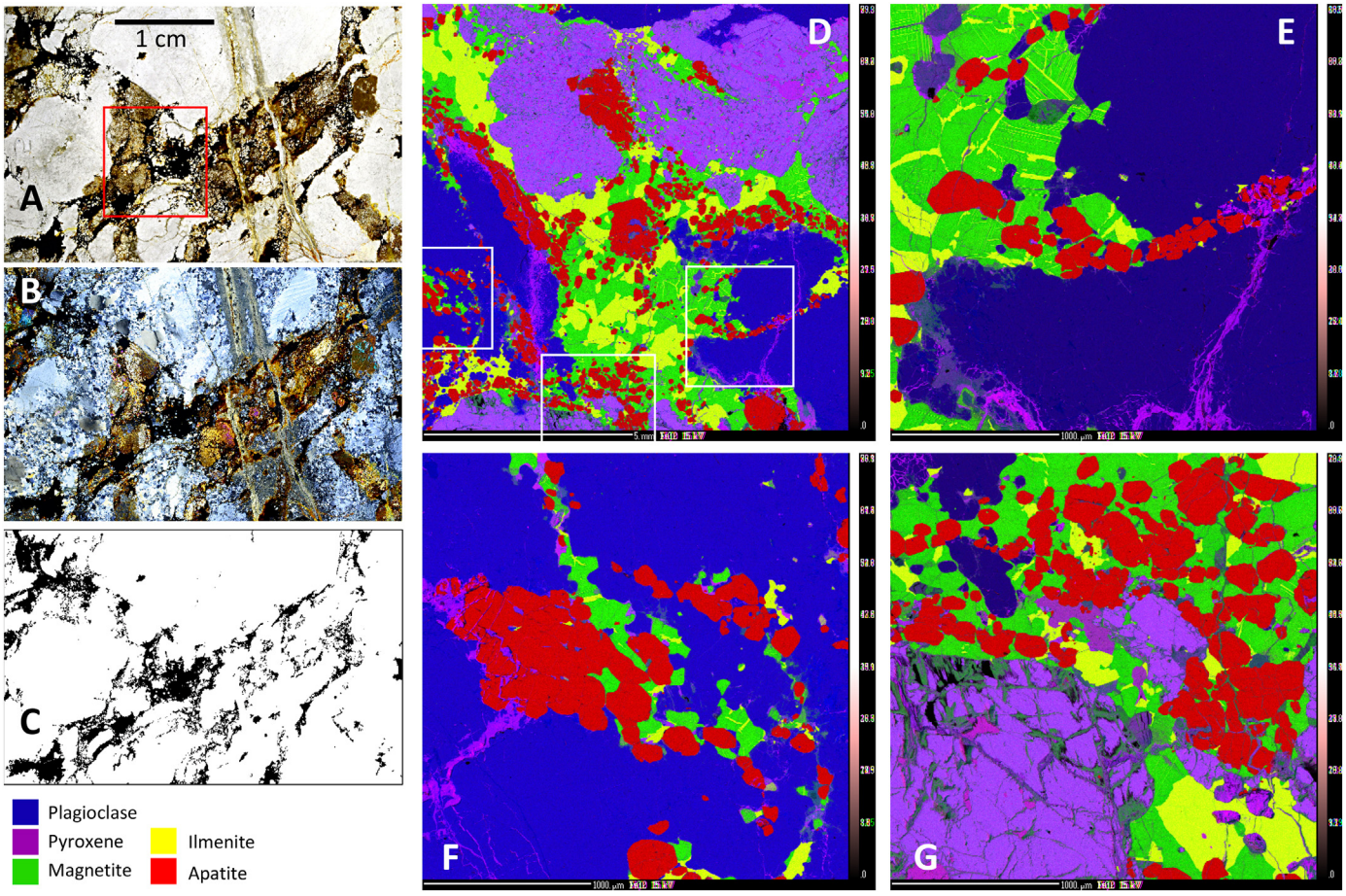

Fig. 8. Cataclastic texture in sample S1925–02. A and B image of the whole thin section in parallel light (A) and crossed nicols (B). C: redraw of the oxide seam to highlight the irregular distribution of the oxides surrounding large cm-sized disrupted clasts crosscutting the mylonitic foliation. D: compositional map after microprobe using the same colour code as in Fig. 5. Apatites are subhedral to euhedral accumulated locally by possible filter pressing at small grain scale. Ox-Ap seams cement brittle fractures in large plagioclase grains (inset E-F). Resorbed rounded plagioclase and pyroxene grains are visible in insets E and G.

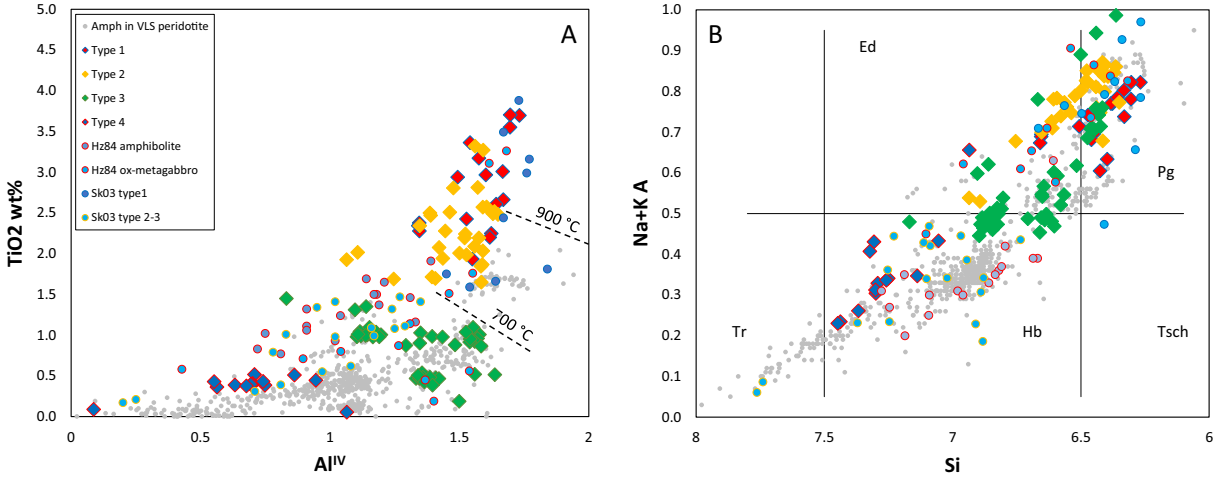

Fig. 9. Compositional variability of the amphiboles in the VLS gabbroids divided by petrographic type as described in the text. Cationic values are calculated based on 23 oxygens. A: TiO_2 vs. Al^{IV}, and B: Na + $K^{(A)}$ vs. Si. Also plotted are the amphiboles from Honnorez et al., 1984 (Hz84) keeping their original subdivision in metagabbros and amphibolites, and those from Skolotnev, 2003 (Sk03). Isotherms are after Ernst and Liu, 1998. Small grey symbols in the background are amphiboles from deformed and undeformed VLS peridotites (Cipriani et al., 2009b). They are representative of hydration during melt infiltration, deformation and metamorphism of the mantle screen rocks in which gabbros are intruded (Cipriani et al., 2009a, 2009b).

magmatic conditions, fixed experimentally at 850–1050 °C (Koepke et al., 2018). On the other hand, amphiboles associated with post-injection deformation (type 3) record slightly lower temperatures (780–900 °C), even though some display clear shifts toward high Al^{IV} and Na + K contents, possibly resulting from incomplete re-equilibration during deformation. In Ca-amphiboles, Al tends to replace Si in tetrahedral coordination with increasing T, whereas it substitutes for Mg + Fe in M2 octahedral site with increasing P (Anderson and Smith, 1995; Gilbert, 1982; Robinson et al., 1982). The low Si contents and high Na + K and Ti are therefore inherited from a high T event linked to the injection of melts saturated in oxides that finally led to the hybridization of the original gabbro matrix. Pertsev et al., 2015 and Ageeva et al. (2017) based on a single oxide gabbro sample from site L2612 (L2612–41), showed that a discrete high-temperature event generated magmatic amphiboles together with precipitation of Fe–Ti oxides in the rock, and that this event was distinct from the continuous magmatic differentiation expected from progressive fractional crystallization. Ageeva and co-workers (2017) revealed co-genetic formation of micrometre-scale needles of Ti–pargasite and Fe–Ti oxides in Cpx. These amphiboles, compositionally akin to type 1, have been interpreted as generated by exsolution from clinopyroxenes in a process involving introduction of Fe via a late magmatic fluid or melt, and micro-scale intra-crystalline redistribution of components (Ageeva et al., 2017).

A precise estimate of the equilibration temperatures can be inferred from amphibole-plagioclase thermometry. Here we applied the calibration of Blundy and Holland, 1990, and Holland and Blundy, 1994, that reveals peak equilibration temperatures between 900 and 950 °C for type 1 amphibole ($P = 2$ kbar) consistent with late magmatic conditions (supplementary Fig. 3).

Peak temperatures >900 °C are present also in type 2–3 amphibole coupled with plagioclase, suggesting that their formation is partly controlled by magmatic fluids. The tail dispersion toward lower T is possibly the effect of progressive cooling and re-equilibration during deformation at decreasing T (supplementary Fig. 3).

Amphiboles of the last group (type 4) are well equilibrated at lower T conditions (700–750 °C, supplementary Fig. 3) indicating a hydrothermal origin, during the same event that caused the pervasive hornblende amphibolitization of these rocks, as described by Honnorez et al. (1984). This last event is isothermal with the closure temperatures of the magnetite-ilmenite system recording very low equilibration temperatures in apparent discordance with the suggested magmatic origin of

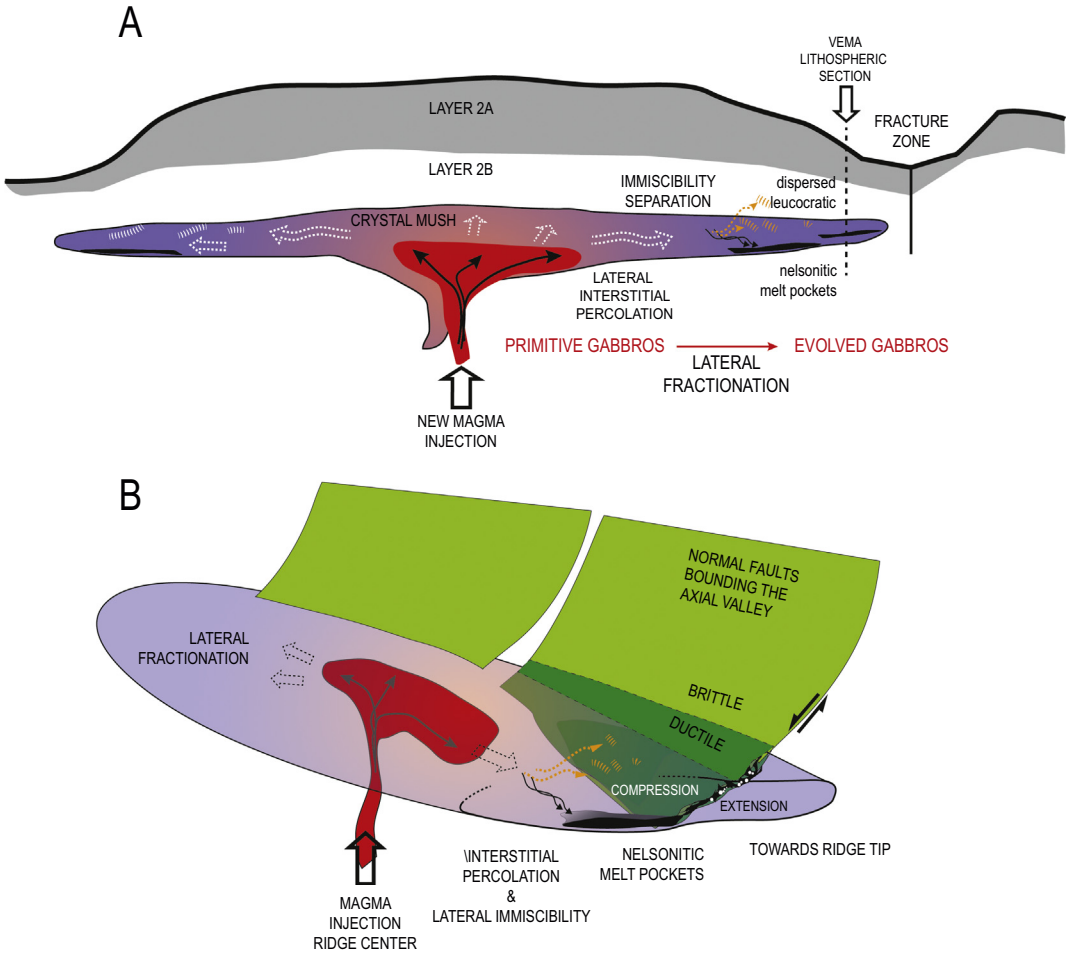

Fig. 10. Schematic representation of the lateral differentiation model proposed here. A: along axis section of the axial magma chamber and lateral interstitial flow (redrawn after Abelson et al., 2001). The flow of magma and crystal mush (black thick arrows) is slower than interstitial flow (white dashed arrows) possibly supported by enhanced pore pressure during magma injection. Gabbros sampled in correspondence of the VLS are representative of the lateral termination of the axial magma chambers and are on average more evolved than ridge-centred gabbros suggesting lateral differentiation. Lateral interstitial reactive differentiation can easily reach the compositional conditions triggering immiscibility. Si-rich and Fe-rich melts follow diverging paths because of different rheological properties. Evolved melt pockets may form at the extremities of the magma chambers. B: rotated 3D cartoon of the interaction of the normal faults bounding the axial valley with the axial magma chamber. The tips of the faults grade into shear zones that are periodically subjected to major dislocations generating a propagation of the brittle deformation into the crystal mush and a coupled compressive-decompressive stress onto the system. Differentiated melts accumulated in these regions can be squeezed out into the shear zones filling the voids generated by brittle fracturing and sealing the cataclastic texture.

these oxides (supplementary Fig. 3). We note, however, that upon cooling, coexisting Ti-magnetite and ilmenite undergo $Fe^{2+}Ti^{4+}$ for $2Fe^{3+}$ exchange, with magnetite gaining Fe^{3+} and ilmenite gaining $Fe^{2+}Ti^{4+}$, shifting both mineral compositions toward the pure endmember composition (Buddington and Lindsley, 1964; Hammond and Taylor, 1982). This process has a low activation energy and therefore the chemical composition of ilmenites and magnetites gives reliable magmatic temperatures only for rocks that underwent rapid cooling as in hypabyssal and extrusive suites (Hammond and Taylor, 1982), while for intrusive rocks the estimated values represent the closure temperature for element exchange in the mineral system.

Textural and thermometric evidence both support injection of extremely differentiated melts into a more primitive crystal mush triggered tectonically. Indeed, deformation may promote pressure gradients that may squeeze a locally accumulated and differentiated melt laterally into a deformed, or still actively deforming, rock. Interstitial melt migration and decompaction suggest a decompressive high-T event, linked to oxide-saturated melt injection.

6.3. Nature of the injected Fe-Ti-P rich melt: evidence for nelsonitic components

Some of the VLS ferrodiorites show apatite enrichments mainly localized within the oxide-rich layers. Exact estimates of the modal mineral proportions within the oxide-rich layers are difficult owing to significant variability at the thin section scale. Moreover, a prolonged melt/rock interaction locally results in mineral resorption and matrix disruption and/or amphibolitization during the hydrous-metamorphic phase. Some samples with a cataclastic texture are more suitable for a definition of the modal proportions, showing larger volumes of oxides filling the clastic network suggesting lower interaction with the matrix. This is the case of sample S1925–02 (Fig. 8) where we estimated a modal proportion of Ap: 0.37, Mag: 0.39 and Ilm: 0.27 (modal counting on SEM images). These values are very close to the modal proportions expected at the eutectic of nelsonitic melts: Ap = 0.3, Fe–Ti Ox = 0.7 (Philpotts, 1967). Nelsonites are Fe–Ti-oxide/apatite-bearing rocks forming ore layers with economic potential in layered intrusions (Charlier et al., 2015 and references therein). The term was initially introduced by Watson and Taber, 1910, for a suite of rocks ranging from rutile-apatite to (hemo-) ilmenite-(Ti-) magnetite-apatite, from the Roseland anorthosite in Virginia. In his recent review Charlier et al. (2015), restricted the use of this term to rocks devoid of silicates. They are generally associated to andesine anorthosites, although the strict correlation of the type of oxide-apatite-bearing melt with a screen rock is not straightforward (Charlier et al., 2015).

Previously discussed textural evidence show that the Fe–Ti–P saturated melt is discordantly injected in the gabbroics along a cataclastic network thus implying the existence of an external reservoir where this melt is accumulated. This reservoir must be large enough to support mechanical extraction of the melt (squeezing), hence suggesting the existence of a physically separated melt pocket or a region of enhanced porosity in the peripheral sector of the axial magma chamber (AMC) where the VLS section cuts the lower crustal intrusions (Fig. 10A).

The need of a separate reservoir for the nelsonitic melt questions the origin and structure of differentiating magma chambers in the axial regions of mid ocean ridges. Modelling fractional crystallization, even when accounting for AFC processes due to reactive melt migration, fails to reproduce the abundance of oxide gabbros in several lower crustal sequences of the MAR (Sanfilippo et al., 2019). In fact, oceanic gabbros are not cumulates sensu stricto, (Irvine, 1982), implying melt mobility albeit at very low melt porosity. Accordingly, much evidence suggests that abyssal gabbros form through an open system crystallization process, in which successive cycles of replenishment and compaction force interstitial melts to migrate and react through a crystal mush in crystal-dominated, rather than magma-dominated, "chambers" (Coumans et al., 2016; Dick et al., 2019; Drouin et al., 2009; Leuthold et al., 2018; Lissenberg et al., 2012, 2019; Lissenberg and Dick, 2008; Lissenberg and MacLeod, 2016; Sanfilippo et al., 2015, 2019; Suhr et al., 2008). During reactive percolation the assimilation of crustal material is so efficient (Kvassnes and Grove, 2008) that it might control the chemical evolution of the migrating magmas (Collier and Kelemen, 2010) producing differentiated melts retaining a 'reactive signature'.

From the experimental viewpoint the formation of Fe–Ti–P saturated melts appears to be favoured by the progressive increase of P in the differentiating melt that results in iron over-enrichment during differentiation due to destabilization of magnetite and progressive increase in modal plagioclase/pyroxene ratio (Charlier and Grove, 2012; Toplis et al., 1994). During reactive migration, interstitial melts are progressively differentiated and, thus, increase their Na–K–Ti and P contents. This differentiation process lowers progressively the liquidus temperature and expands the immiscibility field favouring the intersection of the liquidus with the binodal field where Fe-rich melts separate from Si-rich melts (Bogaerts and Schmidt, 2006; Charlier and Grove, 2012). The silica depletion in the Fe-rich melts in turns favours P saturation as experimentally shown by Tollari et al. (2006) then forcing the formation of highly differentiated melts, as nelsonites, saturated in Fe–Ti oxides and apatite. Moreover, experimental runs on tholeiitic systems showed that the binodal surface can be expanded at hydrous-oxidizing conditions favouring immiscibility in magmatic systems of intermediate evolved composition (Hou et al., 2018). The formation of a distinct nelsonitic reservoir is further favoured by the possible gravitative separation and coalescence of Fe–Ti oxide-saturated melt drops (Natland et al., 1991) considering that Fe-rich melts show a marked density contrast with the surrounding gabbroic mush (Stolper and Walker, 1980).

A problem rising with the immiscibility process is that physical separation of a Fe-rich melt is expected to be coupled to the generation of a Si-rich melt component, not sampled in the VLS lower crust. We propose two possible explanations to this conundrum related to the melt water content:

1) Silica rich melts do not aggregate while Fe-rich ones do. Silica rich melts have higher viscosities than associated basalts, although water addition and superheating can depress their viscosity and allow migration and aggregation (Koepke et al., 2018). Their migration path under the effect of gravity diverge from that of the denser Fe-rich melts and point to the upper part of the crystal mush zone (Natland and Dick, 2002). However, if these Si-rich melts have low water contents, their high viscosity may hinder their migration and local aggregation into physically separated bodies (or veins); their presence would then be recorded as dispersed melt-pockets. Opx-rich (± Am ± Na-rich Pl) patches found in gabbros may be evidence for the reaction of these Si-rich melts with pre-existing crystal mush.

2) Silica-rich melts are squeezed out and assimilated in the surrounding mantle rocks. If water content in the silica-rich fraction is high enough, its mobility may result in lateral intrusions of felsic components into the surrounding rock. Although such lithologies were not recovered among the VLS samples, hydrous melts have been invoked to explain the crystallization of amphibole in mantle peridotites during the shearing event recorded in a large stretch of the VLS mantle section. Shearing resulted in the formation of hybrid mylonitic and ultramylonitic peridotites (Cipriani et al., 2009b). Amphiboles from these rocks are plotted as grey circles in Fig. 9; they concentrate mainly in the hornblende field, but a non-negligible fraction shows edenitic and pargasitic compositions. Overall they have lower Ti content than gabbroic-hosted amphiboles (left panel of Fig. 9), but share similar Na + K, Al^{IV} and silica enrichment. If the evolved melts derived from liquid immiscibility, then they should be depleted in Ti because of its preferential partitioning into the Fe-rich fraction (Charlier and Grove, 2012), followed by the subsequent partitioning of Ti to spinel and pyroxenes in the infiltrated peridotite. In this scenario, the Si-rich melts tend to concentrate at the top of the crustal sequence, possibly squeezed out into the surrounding deforming mantle peridotites, whereas the Fe-rich

fraction laying deeper in the crystal mush might have been squeezed laterally into the adjacent gabbroic mush. This scenario would also explain the "magmatic" Sr–Nd isotope composition of the amphiboles from the VLS peridotite mylonites with values overlapping the field of variability of the VLS MORBs (Cipriani et al., 2009b).

6.4. Melt differentiation is predominantly lateral, not vertical

It is generally assumed that melt flux and differentiation progress mainly in the vertical direction driven by the buoyancy of interstitial melts relative to the general sinking of heavier mineral phases. This assumption contrasts with the observed geometry of the axial magma chambers (AMC) underlying the axis of ridge segments. AMCs in slow-spreading ridges have been clearly detected and studied only at the Thetis Deep in the Red Sea (Ligi et al., 2018) and at the Lucky-Strike segment at 37.2°N along the Mid Atlantic Ridge (Singh et al., 2006). The inferred thickness of the melt-rich layer is possibly in the order of tens of meters, while its lateral extension can span a significant portion of the axial domain, over hundreds of meters to a few kilometres (e.g. Singh et al., 2006). This character is also common in magmatic robust systems where the lower crust is built possibly by progressive multi-sill injections; each single sill is several hundred meters wide, and the lateral length scales at least one or two orders of magnitude larger than thickness (Canales et al., 2000; Canales et al., 2017; Marjanović et al., 2014; Wilcock et al., 2009). Significantly, Abelson et al. (2001) showed that the magmatic foliation of gabbro in the Troodos ofiolites records an intense lateral flux, revealing sub-horizontal magma transport from the centre of the axial ridge toward the tips of the magma chambers approaching the fracture zone. Melt is therefore preferentially delivered to the centre of the segment and moves then toward the tips.

The formation of the VLS by rapid faulting and uplift of the entire lithosphere (Bonatti et al., 2005; Gasperini et al., 2017) exhumed the gabbroic layer unveiling a section representative of the tip of the fossil magma chambers cooled over a 20 Ma time stretch (Fig. 10A). Gabbroids of the VLS, studied here, appear more evolved than gabbros sampled farther away from the fracture zone (Figs. 2 and 3) and are more affected by oxide enrichment as shown above.

We propose here that primitive melts delivered at the centre of the axial segment flow laterally, sustaining a reactive migration of interstitial melts through the host crystal mush. This process favours the crystallization of more evolved lithologies at the peripheral regions of the magma chambers and close to the fracture zone bounding the ridge axis segment. The possible interaction of the mush zone with the roots of active normal faults that bound the rift valleys can tectonically squeeze the evolved melts to hybridize adjacent rocks.

The lateral melt transport can be instantaneously enhanced by injection of primitive magmas at the centre of the axial segment (Fig. 10A). Melt injections increase the pore pressure in the former cooling crystal mushes favouring reactive migration and fractionation of interstitial melts toward the axial tips. Melt flux is progressively replaced by ductile flux of the crystal mush where interstitial melts move faster toward the axial tips (Fig. 10). While favouring the crystallization of more evolved lithologies toward the distal ends of the AMC, this process supports an efficient differentiation of the interstitial melts favouring the separation of Fe-rich melts fostered by immiscibility.

6.5. Mechanics and causes of melt squeezing and injection

Rock textural features described here are common to numerous oceanic gabbroic sequences. For instance, in Hole 735B, Natland and Dick (2001) reported ilmenite-magnetite seams clearly "cementing" gabbroic breccias, thus representing late stage melts injected after rock deformation with no subsequent deformation (Bloomer et al., 1991; John and Cheadle, 2010; Natland et al., 1991; Natland and Dick, 2001). Further examples have been described by MacLeod et al. (2017) in the adjacent Hole 1473A, and seem to be a common feature of the Atlantis Bank gabbros. Based on this evidence, we now suggest that the injection of nelsonitic melts into deforming and/or deformed crystal mushes seen at the VLS may represent the extreme case of a common process of melt reinjection into gabbroic rocks linked to brittle deformation events and to the transmission of stresses at the base of the lithosphere and into melt-rich zones. Since Fe–Ti–P rich melts range from gabbronoritic ($\pm$ Ap $\pm$ Ilm $\pm$ Mag) to nelsonitic (Charlier et al., 2015), their injection may generate a wide variety of different mineral parageneses.

Rock clasts dispersed in the oxide-rich layers indicate that a brittle deformation event responsible for rock fracturing is directly related to high-T melt injection and associated overpressure as discussed earlier. This event is followed by partial dissolution of the host minerals and percolation into grain interstices generating local accumulations by filter separation (Figs. 6 and 8). Based on the observed textures, the last melt/host rock interaction occurred probably at low strain rates, during a phase of relaxation with minor deviatoric stress following melt intrusion. The strong deformation of the injected rocks and the subsequent brittle deformation call for the injection event having occurred at depth, close to the brittle-to-plastic transition. Moreover, the sub-concordance of the ductile and brittle deformation pattern hints at the two deformation regimes differing in intensity/timing but having concordant direction, hence a common cause. A plausible mechanism implies a pulse of deformation, such as a significant slip along one of the major faults bounding the axial ridge domain. At depth the pulse impacts the crust near the brittle-to-plastic transition. Rapid variations in the local stress may force the system to change deformation regimes if it is close to the critical transition point between brittle and plastic regimes. This results in the propagation of the brittle deformation into the ductile domain during the impulse. The candidate region is the crustal volume at the level of the AMC underlying the rift valley floor where crustal faults progressively grade into ductile shear zones at or near the edges of the AMC (Fig. 10). Such a geometry has been inferred at the Lucky Strike segment, where rift bounding faults have been imaged at depths approaching the axial magma chamber (Combier et al., 2015; Dusunur et al., 2009; Singh et al., 2006). Here, the seismic reflectors reveal the presence of a thin low-velocity zone forming a sill-like structure at the base of the lithosphere. The tip of the ridge-bounding faults approach closely the top of the AMC (Dusunur et al., 2009) possibly marking the local transition to plastic deformation. Microseismicity around the AMC at Lucky Strike reveals that the hanging wall block displays mainly compressive events attributed to contractional hydrothermal-driven cooling of this part of the crust (Crawford et al., 2013; Dusunur et al., 2009). Although not documented to date, similar interactions can be expected for detachment faults reaching deep into the lithosphere as in oceanic core complexes. The lack of oceanic detachments along the VTR (supplementary Fig. 1) indicates instead that the *E*-MAR segment, where the VLS gabbros have been emplaced, results from 'classical', symmetric oceanic accretion with relatively robust melt supply. In this mode of accretion, tectonic extension is accommodated by ridge-parallel normal faults and by a steady-state rift valley. We expect hence that these bounding faults have been present throughout the whole accretion history, and that they successively interacted with the lower crust and every newly formed AMCs.

Further insights into the interaction between faulting and AMC can be gained from both modelling of fault deformation and from observations at fast-spreading ridges. Modelling the shear-induced internal deformation field associated to tensile faults predicts compression stress shadows on the hanging wall and at the base (tip) of the fault, while extension is expected along the adjacent footwall (e.g. Okada, 1992). On the other hand, the intrusion of an overpressured axial sill can modify the stress field, promoting reverse faulting at the edges of the injected sill coupled with normal faulting above it (Wilcock et al., 2009). This geometry has been observed at the Endeavour ridge segment along the Juan de Fuca Ridge (Pacific Ocean), based on micro-seismicity fault-plane solutions around the AMC. Brittle events were located in close proximity to the AMC (tens of meters) with normal and reverse faulting narrowly bounding the AMC reflector (Wilcock et al., 2009).

We anticipate similar stress patterns near the roots of major fault systems at slow- and ultra-slow ridges. The observations at the Lucky Strike segment (Crawford et al., 2013; Dusunur et al., 2009), at the Endeavour ridge (Wilcock et al., 2009) and modelling (e.g. Okada, 1992) coherently show that the stress field at the tip of the fault has an overpressure component on the hanging wall area, and dilation on the footwall block. This stress pattern can thus generate a pressure gradient that could drive melt from the hanging wall to the footwall, and likely interact with shear deformation at the root of the fault. Melt remobilization in this context, and in proximity to the brittle-plastic transition, is compatible with the observed matrix deformation (pre- and post- injection), and with melt-driven fracturing due to overpressure, melt-enhanced strain localization, or both. This scenario, depicted in Fig. 10B, would be consistent with the observed normal faults rooting in close proximity to the melt-rich AMC (Crawford et al., 2013; Dusunur et al., 2009; Singh et al., 2006; Wilcock et al., 2009).

Compressional stresses, mainly located on the hanging wall block and at the tip of the fault can generate rapid squeezing of existing melt pockets or of the melt distributed in the residual porosity. The concomitant decompressional stress pattern in the footwall region enhances the pressure gradient favouring melt injections that will be driven preferentially into the sheared region.

Two concurrent tectono-magmatic components act during such a process: the interplay between melt accumulation, shearing and rock rheology and the interference between magma chambers (crystal mushes) and the root of the faulting system at ridge axis. Deformation-induced melt concentration along shear zones has been documented at Atlantis Bank (Dick et al., 1991a, 1991b, 2019) as well as in experimental studies and in field observations in ophiolites (Hirth and Kohlstedt, 1995; Kaczmarek and Tommasi, 2011; Kelemen and Dick, 1995), and is also observed in other magmatic environments such as granitic intrusions (Rosenberg and Handy, 2005). Deformation experiments show that during plastic deformation melts may be both concentrated and extracted, with inhomogeneous compaction and expansion of the deforming sample (e.g. Holtzman et al., 2012).

However, none of these experiments replicate the clastic textures discussed here, that still occur at elevated temperatures. Owing to variations in permeability and connectivity of melt in these samples, the overpressure may induce melt injection, involving compression and squeezing of a melt reservoir. Melt squeezing can cause local overpressurization, thus a reduction of the effective confining pressure, in turn promoting semi-brittle or brittle fracturing (akin to hydrofracturing).

Experiments also show that a rheological 'solid-to-liquid' transition occurs at a critical melt content threshold (e.g. Hirth and Kohlstedt, 2003; Rosenberg and Handy, 2005). Hence, melt percolation associated with deformation can result locally in significant melt-induced weakening, promoting at the same time higher strain rates, and therefore a transition from ductile to semi-brittle or brittle deformation of the host rock.

It is worth recalling at the end of this discussion that Bowen (1920) predicted that differentiation by crystallization could be driven by deformation of crystal mushes resulting in the formation of adcumulates of extreme purity (*"…For anorthosites, by way of example, it is probable that, besides the sorting of plagioclase crystals by gravitative action, a squeezing out of the interstitial liquid may have contributed to their extreme purity in many cases…"*).

7. Summary and concluding remarks

The study of the lower crustal section at the Vema Lithospheric Section allowed recognition of magmatic and tectonic processes occurring at the tips of magma intrusions in the lower oceanic crust. Highly differentiated magma pockets at the edges of axial magma chambers may be squeezed mechanically and injected into the surrounding rocks. The main points discussed here can be summarized as follows:

- Gabbros sampled along the Vema Lithospheric Section (VLS) are on average more evolved than those from other axial regions of Mid Ocean Ridges. The Vema Lithospheric Section dissects the lateral termination of the axial magma chambers, thus suggesting lateral magmatic differentiation with primitive melts preferentially injected at the centre of ridge segments.
- Oxide-rich gabbroids (ferrodiorites) from the Vema Lithospheric Section are hybrid rocks formed by overpressured injection of highly differentiated melts (saturated in Fe–Ti oxides and apatite) within mylonitized gabbroics of more primitive composition.
- Oxide-rich layers are associated to intense brittle fracturing of a pre-existing mylonitized groundmass. Rock clasts dispersed in the oxide layers reveal melt overpressure and "hydrofracturing" occurring at elevated temperatures. Subsequently the host rock records partial dissolution and decompaction of the mineral assemblage.
- The injected melts are compositionally akin to nelsonitic melts known from continental layered intrusions. Melt injection is recorded by the crystallization of Fe–Ti oxides and apatite ± Na–plagioclase and clinopyroxene in large mineral interstices and newly formed cracks.
- The occurrence of such extremely differentiated melts can be related to lateral differentiation by reactive melt migration through a primitive crystal mush from the centre to the lateral termination of an axial magma chamber. The differentiation process is enhanced by melt immiscibility during lateral transport.
- Melt injection may be related to stress patterns associated with faults rooting near melt-rich zones and associated with crustal volumes at or near the brittle-to-plastic transition. Fault-induced changes of the stress regime may drive focused melt migration in turn leading to overpressure, and/or to enhanced strain localization resulting in higher strain rates. Both processes may promote a pressure-driven shift from plastic to semi-brittle or brittle deformation, consistent with microtextural evidence.

Declaration of Competing Interest

The authors declare that they have no known competing financial interests or personal relationships that could have appeared to influence the work reported in this paper.

Acknowledgments

This study was supported by the Italian Programma di Rilevante Interesse Nazionale (PRIN_2017KY5ZX8) and by Accordo Bilaterale CNR/RFBR 2018-2020. AC is supported by Programma di Rilevante Interesse Nazionale PRIN 20178LPCPW. We are grateful to M. Fialin and N. Rividi for their help at the CAMPARIS analytical service, Paris. The manuscript has benefited from the precious reviews of Henry Dick, Akihiro Tamura and two anonymous reviewers and the careful editorial support of Theo Ntaflos and Costanza Bonadiman. I gratefully thankyou Jurgen's firm opposition to immiscibility and Mike's infinite chocolate reservoir that warmly accompanied us across the Atlantic.

Appendix A. Supplementary data

Supplementary data to this article can be found online at https://doi.org/10.1016/j.lithos.2020.105589.

References

Abelson, M., Baer, G., Agnon, A., 2001. Evidence from gabbro of the Troodos ophiolite for lateral magma transport along a slow-spreading mid-ocean ridge. Nature 409, 72–75. https://doi.org/10.1038/35051058.

Ageeva, O., Habler, G., Pertsev, A., Abart, R., 2017. Fe-Ti oxide micro-inclusions in clinopyroxene of oceanic gabbro: phase content, orientation relations and petrogenetic implication. Lithos 290, 104–115.

Anderson, J.L., Smith, D.R., 1995. The effects of temperature and f O2 on the Al-in-hornblende barometer. Am. Mineral. 80, 549–559.

Atkinson, B.K., 1977. The kinetics of ore deformation: its illustration and analysis by means of deformation-mechanism maps. Geol. Föreningen i Stock. Förhandlingar 99, 186–197.

Auzende, J.-M., Bideau, D., Bonatti, E., Cannat, M., Honnorez, J., Lagabrielle, Y., Malavieille, J., Mamaloukas-Frangoulis, V., Mevel, C., 1989. Direct observation of a section through slow-spreading oceanic crust.pdf. Nature 337, 726.

Auzende, J.M., Bideau, D., Bonatti, E., Cannat, M., Honnorez, J., Lagabrielle, Y., Malavieille, J., Mamaloukas-Frangoulis, V., Mével, C., 1990. The MAR-Vema Fracture Zone intersection surveyed by deep submersible Nautile. Terra Nova 2, 68–73. https://doi.org/10.1111/j.1365-3121.1990.tb00038.x.

Blackman, D.K., Ildefonse, B., John, B.E., Ohara, Y., Miller, D.J., MacLeod, C.J., 2006. The expedition 304/305 scientists (2006). Proceedings of the integrated ocean drilling program. 304, p. 305.

Bloomer, S.H., Meyer, P.S., Dick, H.J.B., Ozawa, K., Natland, J.H., 1991. Textural and mineralogical variations in gabbroic rocks from hole 735B. In: Von Herzen, R.P., Robinson, P.T., et al. (Eds.), Proc. ODP, Sci. Results, pp. 21–39.

Blundy, J.D., Holland, T.J.B., 1990. Calcic amphibole equilibria and a new amphibole-plagioclase geothermometer. Contrib. Mineral. Petrol. 104, 208–224. https://doi.org/10.1007/BF00306444.

Bogaerts, M., Schmidt, M.W., 2006. Experiments on silicate melt immiscibility in the system Fe 2 SiO 4–KAlSi 3 O 8–SiO 2–CaO–MgO–TiO 2–P 2 O 5 and implications for natural magmas. Contrib. Mineral. Petrol. 152, 257–274.

Bonatti, E., 1978. Vertical tectonism in oceanic fracture zones. Earth Planet. Sci. Lett. 37, 369–379.

Bonatti, E., Ligi, M., Brunelli, D., Cipriani, A., Fabretti, P., Ferrante, V., Gasperini, L., Ottolini, L., 2003. Mantle thermal pulses below the Mid-Atlantic Ridge and temporal variations in the formation of oceanic lithosphere. Nature 423, 499–505. https://doi.org/10.1038/nature01594.

Bonatti, E., Brunelli, D., Buck, W.R., Cipriani, A., Fabretti, P., Ferrante, V., Gasperini, L., Ligi, M., 2005. Flexural uplift of a lithospheric slab near the Vema transform (Central Atlantic): timing and mechanisms. Earth Planet. Sci. Lett. 240, 642–655. https://doi.org/10.1016/j.epsl.2005.10.010.

Bowen, N.L., 1920. Differentiation by deformation. Proc. Natl. Acad. Sci. U. S. A. 6, 159.

Brunelli, D., Seyler, M., Cipriani, A., Ottolini, L., Bonatti, E., 2006. Discontinuous Melt Extraction and Weak Refertilization of Mantle Peridotites at the Vema Lithospheric Section (Mid-Atlantic Ridge). J. Petrol. 47, 745–771. https://doi.org/10.1093/petrology/egi092.

Brunelli, D., Cipriani, A., Bonatti, E., 2018. Thermal effects of pyroxenites on mantle melting below mid-ocean ridges. Nat. Geosci. 37. https://doi.org/10.1038/s41561-018-0139-z.

Buddington, A.F., Lindsley, D.H., 1964. Iron-titanium oxide minerals and synthetic equivalents. J. Petrol. 5, 310–357.

Canales, J.P., Collins, J.A., Escartín, J., Detrick, R.S., 2000. Seismic structure across the rift valley of the Mid-Atlantic Ridge at 23 20′ (MARK area): Implications for crustal accretion processes at slow spreading ridges. J. Geophys. Res. Solid Earth 105, 28411–28425.

Canales, J.P., Dunn, R.A., Arai, R., Sohn, R.A., 2017. Seismic imaging of magma sills beneath an ultramafic-hosted hydrothermal system. Geology 45, 451–454.

Cande, S.C., Kent, D.V., 1995. Revised calibration of the geomagnetic polarity time scale for the late cretaceous and Cenozoic. J. Geophys. Res. 100, 6093–6095. https://doi.org/10.1029/94JB03098.

Cannat, M., Mamaloukas-Frangoulis, V., Auzende, J.-M., Bideau, D., Bonatti, E., Honnorez, J., Lagabrielle, Y., Malavieille, J., Mevel, C., 1991. A geological cross-section of the Vema fracture zone transverse ridge, Atlantic Ocean. J. Geodyn. 13, 97–117. https://doi.org/10.1016/0264-3707(91)90034-C.

Charlier, B., Grove, T.L., 2012. Experiments on liquid immiscibility along tholeiitic liquid lines of descent. Contrib. Mineral. Petrol. 164, 27–44.

Charlier, B., Sakoma, E., Sauvé, M., Stanaway, K., Vander Auwera, J., Duchesne, J.C., 2008. The Grader layered intrusion (Havre-Saint-Pierre Anorthosite, Quebec) and genesis of nelsonite and other Fe–Ti–P ores. Lithos 101 (3-4), 359–378.

Charlier, B., Namur, O., Bolle, O., Latypov, R., Duchesne, J.-C., 2015. Fe-Ti-V-P ore deposits associated with Proterozoic massif-type anorthosites and related rocks. EarthSci. Rev. 141, 56–81. https://doi.org/10.1016/j.earscirev.2014.11.005.

Cipriani, A., Bonatti, E., Brunelli, D., Ligi, M., 2009a. 26 million years of mantle upwelling below a segment of the Mid Atlantic Ridge: the Vema Lithospheric Section revisited. Earth Planet. Sci. Lett. 285, 87–95. https://doi.org/10.1016/j.epsl.2009.05.046.

Cipriani, A., Bonatti, E., Seyler, M., Brueckner, H.K., Brunelli, D., Dallai, L., Hemming, S.R., Ligi, M., Ottolini, L., Turrin, B.D., 2009b. A 19 to 17 Ma amagmatic extension event at the Mid-Atlantic Ridge: Ultramafic mylonites from the Vema Lithospheric Section. Geochem. Geophys. Geosyst. 10, 1–53. https://doi.org/10.1029/2009GC002534.

Cipriani, A., Brueckner, H.K., Bonatti, E., Brunelli, D., 2004. Oceanic crust generated by elusive parents: Sr and Nd isotopes in basalt-peridotite pairs from the Mid-Atlantic Ridge. Geology 32, 657–660.

Collier, M.L., Kelemen, P.B., 2010. The Case for Reactive Crystallization at Mid-Ocean Ridges. J. Petrol. 51, 1913–1940. https://doi.org/10.1093/petrology/egq043.

Combier, V., Seher, T., Singh, S.C., Crawford, W.C., Cannat, M., Escartín, J., Dusunur, D., 2015. Three-dimensional geometry of axial magma chamber roof and faults at Lucky Strike volcano on the Mid-Atlantic Ridge. J. Geophy. Res. B: Solid Earth 120 (8). https://doi.org/10.1002/2015JB012365.

Coumans, J.P., Stix, J., Clague, D.A., Minarik, W.G., Layne, G.D., 2016. Melt-rock interaction near the Moho: evidence from crystal cargo in lavas from near-ridge seamounts. Geochim. Cosmochim. Acta 191, 139–164.

Crawford, W.C., Rai, A., Singh, S.C., Cannat, M., Escartin, J., Wang, H., Daniel, R., Combier, V., 2013. Hydrothermal seismicity beneath the summit of Lucky strike volcano, Mid-Atlantic Ridge. Earth Planet. Sci. Lett. 373, 118–128.

Danyushevsky, L.V., Plechov, P., 2011. Petrolog3: Integrated software for modeling crystallization processes. Geochemistry, Geophysics. Geosystems 12 (7). https://doi.org/10.2973/odp.proc.sr.118.128.1991.

Dick, H.J.B., Meyer, P.S., Bloomer, S., Kirby, S., Stakes, D., Mawer, C., 1991a. Lithostratigraphic evolution of an in situ section of oceanic layer 3. Proc. Ocean Drill. Progr. Sci. Results 118, 439–538. https://doi.org/10.2973/odp.proc.sr.118.128.1991.

Dick, H.J.B., Schouten, H., Meyer, P.S., Gallo, D.G., Berg, H., Tyce, R., Patriat, P., Johnson, K., Snow, J., Fisher, A., 1991b. Bathymetric map of the Atlantis II Fracture Zone, Southwest Indian Ridge. In: Von Herzen, R.P., Robinson, P.T., et al. (Eds.), Proc. ODP, Sci. Results.

Dick, H.J.B., Natland, J.H., Alt, J.C., Bach, W., Bideau, D., Gee, J.S., Haggas, S., Hertogen, J.G.H., Hirth, G., Holm, P.M., Ildefonse, B., Iturrino, G.J., John, B.E., Kelley, D.S., Kikawa, E., Kingdon, A., LeRoux, P.J., Maeda, J., Meyer, P.S., Miller, D.J., Naslund, H.R., Niu, Y.-L., Robinson, P.T., Snow, J., Stephen, R.A., Trimby, P.W., Worm, H.-U., Yoshinobu, A., 2000. A long in situ section of the lower ocean crust: results of ODP Leg 176 drilling at the Southwest Indian Ridge. Earth Planet. Sci. Lett. 179, 31–51. https://doi.org/10.1016/s0012-821x(00)00102-3.

Dick, H.J.B., MacLeod, C.J., Blum, P., Abe, N., Blackman, D.K., Bowles, J.A., Cheadle, M.J., Cho, K., Ciążela, J., Deans, J.R., Edgcomb, V.P., Ferrando, C., France, L., Ghosh, B., Ildefonse, B., John, B., Kendrick, M.A., Koepke, J., Leong, J.A.M., Liu, C., Ma, Q., Morishita, T., Morris, A., Natland, J.H., Nozaka, T., Pluemper, O., Sanfilippo, A., Sylvan, J.B., Tivey, M.A., Tribuzio, R., Viegas, G., 2019. Dynamic accretion beneath a Slow-spreading ridge segment: IODP Hole 1473A and the Atlantis Bank Oceanic Core complex. J. Geophys. Res. Solid Earth 2020. https://doi.org/10.1029/2018JB016858.

Drouin, M., Godard, M., Ildefonse, B., Bruguier, O., Garrido, C.J., 2009. Geochemical and petrographic evidence for magmatic impregnation in the oceanic lithosphere at Atlantis Massif, Mid-Atlantic Ridge (IODP Hole U1309D, 30°N). Chem. Geol. 264, 71–88. https://doi.org/10.1016/j.chemgeo.2009.02.013.

Dusunur, D., Escartín, J., Combier, V., Seher, T., Crawford, W., Cannat, M., Singh, S.C., Matias, L.M., Miranda, J.M., 2009. Seismological constraints on the thermal structure along the Lucky strike segment (Mid-Atlantic Ridge) and interaction of tectonic and magmatic processes around the magma chamber. Mar. Geophys. Res. 30, 105–120.

Ernst, W.G., Liu, J., 1998. Experimental phase-equilibrium study of Al- and Ti-contents of calcic amphibole in MORB; a semiquantitative thermobarometer. Am. Mineral. 83, 952–969. https://doi.org/10.2138/am-1998-9-1004.

Fabretti, P., Bonatti, E., Peyve, A., Brunelli, D., Cipriani, A., Dobrolubova, X., Efimov, V., Erofeev, S., Gasperini, L., Hanley, J.E., Ligi, M., Perfiliev, A., Rastorguyev, V., Raznitsin, Y., Savelieva, G., Semjenov, V., Simonov, V., Sokolov, S., Skolotnev, S., Susini, S., Vikentyev, I., 1998. First results of cruise S19 (PRIMAR project): Petrological and structural investigations of the Vema transverse ridge (equatorial Atlantic). G. di Geol. 60.

Gasperini, L., Bonatti, E., Borsetti, A.M., Capotondi, L., Cipriani, A., Negri, A., 2017. Timing of transverse ridge uplift along the Vema transform (Central Atlantic). Mar. Geol. 385, 228–232 ISSN: 0025–3227.

Gilbert, M.C., 1982. Experimental studies of amphibole stability. Rev. Mineral. 9, 229–346.

Hammond, P.A., Taylor, L.A., 1982. The ilmenite/titano-magnetite assemblage: kinetics of re-equilibration. Earth Planet. Sci. Lett. 61, 143–150. https://doi.org/10.1016/0012-821X(82)90047-4.

Heezen, B.C., Gerard, R.D., Tharp, M., 1964. The Vema Fracture Zone in the equatorial Atlantic. J. Geophys. Res. 69, 733–739.

Hirth, G., Kohlstedt, D.L., 1995. Experimental constraints on the dynamics of the partially molten upper mantle: Deformation in the diffusion creep regime. J. Geophys. Res. Solid Earth 100, 1981–2001.

Hirth, G., Kohlstedt, D., 2003. Rheology of the upper mantle and the mantle wedge: a view from the experimentalists. Insid. Subduction Fact. 83–105.

Holland, T., Blundy, J., 1994. Non-ideal interactions in calcic amphiboles and their bearing on amphibole-plagioclase thermometry. Contrib. Mineral. Petrol. 116, 433–447. https://doi.org/10.1007/BF00310910.

Holtzman, B.K., King, D.S.H., Kohlstedt, D.L., 2012. Effects of stress-driven melt segregation on the viscosity of rocks. Earth Planet. Sci. Lett. 359, 184–193.

Honnorez, J., Mével, C., Montigny, R., 1984. Geotectonic significance of gneissic amphibolites from the Vema fracture zone, equatorial Mid-Atlantic Ridge. J. Geophys. Res. 89, 11379–11400.

Hou, T., Charlier, B., Holtz, F., Veksler, I., Zhang, Z., Thomas, R., Namur, O., 2018. Immiscible hydrous Fe–Ca–P melt and the origin of iron oxide-apatite ore deposits. Nat. Commun. 9 (1), 1–8.

Irvine, T.N., 1982. Terminology for layered intrusions. J. Petrol. 23, 127–162.

John, B.E., Cheadle, M.J., 2010. Deformation and alteration associated with oceanic and continental detachment fault systems: are they similar. Divers. Hydrothermal Syst. Slow Spreading Ocean Ridges, Geophys. Monogr. Ser 188, 175–206.

Kaczmarek, M., Tommasi, A., 2011. Anatomy of an extensional shear zone in the mantle, Lanzo massif, Italy. Geochem. Geophys. Geosyst. 12.

Kastens, K., Bonatti, E., Caress, D., Carrara, G., Dauteuil, O., Frueh-Green, G., Ligi, M., Tartarotti, P., 1998. The Vema transverse ridge (Central Atlantic). Mar. Geophys. Res. 20, 533–556.

Kelemen, P.B., Dick, H.J.B., 1995. Focused melt flow and localized deformation in the upper mantle: Juxtaposition of replacive dunite and ductile shear zones in the Josephine peridotite, SW Oregon. J. Geophys. Res. Solid Earth 100, 423–438.

Koepke, J., Botcharnikov, R.E.E., Natland, J.H.J.H., 2018. Crystallization of late-stage MORB under varying water activities and redox conditions: Implications for the formation of highly evolved lavas and oxide gabbro in the ocean crust. Lithos 323, 58–77. https://doi.org/10.1016/j.lithos.2018.10.001.

Kostitsyn, Y.A., Silantyev, S.A., Anosova, M.O., Shabykova, V.V., Skolotnev, S.G., 2018. Age of Plutonic Rocks from the Vema Fracture Zone (Central Atlantic) and Nature of their Mantle sources. Geochem. Int. 56, 89–110. https://doi.org/10.1134/s0016702918020039.

Kvassnes, A.J.S., Grove, T.L., 2008. How partial melts of mafic lower crust affect ascending magmas at oceanic ridges. Contrib. Mineral. Petrol. 156, 49–71.

Le Maitre, R.W., Streckeisen, A., Zanettin, B., Le Bas, M.J., Bonin, B., Bateman, P., Bellieni, G., Dudek, A., Efremova, S., Keller, J., Lameyre, J., Sabine, P.A., Schmid, R., Sorensen, H., Wooley, A.R., 2002. A classification of igneous rocks and glossary of terms. J. Volcanol. Geotherm. Res., Second ed. Cambridge University Press, Cambridge. https://doi.org/10.1016/0377-0273(91)90012-o

Leuthold, J., Lissenberg, C.J., O'Driscoll, B., Karakas, O., Falloon, T., Klimentyeva, D.N., Ulmer, P., 2018. Partial melting of lower oceanic crust gabbro: constraints from poikilitic clinopyroxene primocrysts. Front. Earth Sci. 6, 15.

Ligi, M., Bonatti, E., Bosworth, W., Cai, Y., Cipriani, A., Palmiotto, C., Ronca, S., Seyler, M., 2018. Birth of an ocean in the Red Sea: Oceanic-type basaltic melt intrusions precede continental rupture. Gondwana Res. 54, 150–160. https://doi.org/10.1016/j.gr.2017.11.002.

Lissenberg, C.J., Dick, H.J.B., 2008. Melt-rock reaction in the lower oceanic crust and its implications for the genesis of mid-ocean ridge basalt. Earth Planet. Sci. Lett. 271, 311–325. https://doi.org/10.1016/j.epsl.2008.04.023.

Lissenberg, C.J., MacLeod, C.J., 2016. A reactive porous flow control on mid-ocean ridge magmatic evolution. J. Petrol. 57, 2195–2220.

Lissenberg, C.J., Rioux, M., Shimizu, N., Bowring, S.A., Mével, C., 2009. Zircon dating of oceanic crustal accretion. Science 323, 1048–1050. https://doi.org/10.1126/science.1167330.

Lissenberg, C.J., Macleod, C.J., Howard, K.A., Godard, M., 2012. Pervasive Reactive Melt Migration Through fast-Spreading Lower Oceanic Crust (Hess Deep , Equatorial Pacific Ocean).

Lissenberg, C.J., MacLeod, C.J., Bennett, E.N., 2019. Consequences of a crystal mush-dominated magma plumbing system: a mid-ocean ridge perspective. Philos.Trans. R. Soc. A 377, 20180014.

MacLeod, C.J., Dick, H.J.B., Blum, P., Abe, N., Blackman, D.K., Bowles, J.A., Cheadle, M.J., Cho, K., Ciążela, J., Deans, J.R., 2017. Hole 1105A redescription. Proc. Int. Ocean Discov. Progr. 360.

Marjanović, M., Carbotte, S.M., Carton, H., Nedimović, M.R., Mutter, J.C., Canales, J.P., 2014. A multi-sill magma plumbing system beneath the axis of the East Pacific Rise. Nat. Geosci. 7 (11), 825–829. https://doi.org/10.1038/ngeo2272.

Matzen, A.K., Baker, M.B., Beckett, J.R., Stolper, E.M., 2013. The temperature and pressure dependence of nickel partitioning between olivine and silicate melt. J. Petrol. 54, 2521–2545.

Mazzucchelli, M., 2016. Classification of Igneous Rocks: Diorite Vs. Syenite - A Suggestion to Avoid a Contradiction. Episodes 39, 524. https://doi.org/10.18814/epiiugs/2016/v39i3/100890.

Miranda, E.A., John, B.E., 2010. Strain localization along the Atlantis Bank oceanic detachment fault system, Southwest Indian Ridge. Geochem. Geophys. Geosyst. 11. https://doi.org/10.1029/2009GC002646.

Natland, J.H., Dick, H.J.B., 2001. Formation of the lower ocean crust and the crystallization of gabbroic cumulates at a very slowly spreading ridge. J. Volcanol. Geotherm. Res. 110, 191–233. https://doi.org/10.1016/S0377-0273(01)00211-6.

Natland, J.H., Dick, H.J.B., 2002. Stratigraphy and composition of gabbros drilled in Ocean Drilling Program Hole 735B, Southwest Indian Ridge: A synthesis of geochemical data. Proceedings of the Ocean Drilling Program, Scientific Results. College Station, TX (Ocean Drilling Program), pp. 1–69.

Natland, J.H., Meyer, P.S., Dick, H.J.B., Bloomer, S.H., 1991. Magmatic oxides and sulfides in gabbroic rocks from Hole 735B and the later development of the liquid line of descent. In: Von Herzen, R.P., Robinson, P.T., et al. (Eds.), Proc. ODP Sci. Results, pp. 75–111.

Okada, Y., 1992. Internal deformation due to shear and tensile faults in a half-space. Bull. Seismol. Soc. Am. 82, 1018–1040.

Pertsev, A.N., Aranovich, L.Y., Prokofiev, V.Y., Bortnikov, N.S., Cipriani, A., Simakin, S.S., Borisovskiy, S.E., 2015. Signatures of residual melts, magmatic and seawater-derived fluids in oceanic lower-crust gabbro from the Vema lithospheric section, Central Atlantic. J. Petrol. 56, 1069–1088.

Pettigrew, T.J., Casey, J.F., Miller, D.J., Araki, E., Boissonnas, R., Busby, R., Einaudi, F., Gerdom, M., Guo, Z.P., Hopkins, H., 1999. Leg 179 summary. Proc. Ocean Drill. Program Initial Rep. Citeseer, p. 26.

Philpotts, A.R., 1967. Origin of certain iron-titanium oxide and apatite rocks. Econ. Geol. 62, 303–315. https://doi.org/10.2113/gsecongeo.62.3.303.

Rioux, M., Jons, N., Bowring, S., Lissenberg, C.J., Bach, W., Kylander-Clark, A., Hacker, B., Dudas, F., 2015. U-Pb dating of interspersed gabbroic magmatism and hydrothermal metamorphism during lower crustal accretion, Vema lithospheric section, Mid-Atlantic Ridge. J. Geophys. Res. 120, 2093–2118. https://doi.org/10.1002/2014JB011668.

Robinson, P., Doolan, B.L., Schumacher, J.C., 1982. Chapter 1, phase relations of metamorphic amphiboles; natural occurrence and theory; General review of metamorphic amphibole compositions; composition space of metamorphic amphiboles and its population. Rev. Mineral. Geochem. 9, 22–43.

Roduit, N., 2019. Image Analysis Toolbox for Measuring and Quantifying Components of High-Definition Images. Version 1.3.1. https://jmicrovision.github.io.

Rosenberg, C.L., Handy, M.R., 2001. Mechanisms and orientation of melt segregation paths during pure shearing of a partially molten rock analog (norcamphor–benzamide). J. Struct. Geol. 23, 1917–1932. https://doi.org/10.1016/S0191-8141(01)00037-2.

Rosenberg, C.L., Handy, M.R., 2005. Experimental deformation of partially melted granite revisited: implications for the continental crust. J. Metamorph. Geol. 23, 19–28.

Ryan, W.B.F., Carbotte, S.M., Coplan, J., O'Hara, S., Melkonian, A., Arko, R., Weissel, R.A., Ferrini, V., Goodwillie, A., Nitsche, F., Bonczkowski, J., Zemsky, R., 2009. Global Multi-Resolution Topography (GMRT) synthesis data set. Geochem. Geophys. Geosyst. 10, Q03014. https://doi.org/10.1029/2008GC002012.

Sanfilippo, A., Dick, H.J.B., OHara, Y., 2013. Melt-Rock Reaction in the Mantle: Mantle Troctolites from the Parece Vela Ancient Back-Arc Spreading Center. J. Petrol. 54, 861–885. https://doi.org/10.1093/petrology/egs089.

Sanfilippo, A., Tribuzio, R., Tiepolo, M., Berno, D., 2015. Reactive flow as dominant evolution process in the lowermost oceanic crust: evidence from olivine of the Pineto ophiolite (Corsica). Contrib. Mineral. Petrol. 170, 38.

Sanfilippo, A., Dick, H.J.B., Marschall, H.R., Lissenberg, C.J., Urann, B., 2019. Emplacement and high-temperature evolution of gabbros of the 16.5°N Oceanic core complexes (Mid-Atlantic Ridge): insights into the compositional Variability of the lower Oceanic Crust. Geochem. Geophys. Geosyst. 20, 46–66. https://doi.org/10.1029/2018GC007512.

Seyler, M., Brunelli, D., 2018. Sodium-chromium covariation in residual clinopyroxenes from abyssal peridotites sampled in the 43°–46° E region of the Southwest Indian Ridge. Lithos 302, 142–157.

Shaw, P.R., Cande, S.C., 1990. High-resolution Inversion for South Atlantic plate kinematics using Joint altimeter and magnetic anomaly data. J. Geophys. Res. 95, 2625–2644.

Singh, S.C., Crawford, W.C., Carton, H., Seher, T., Combier, V., Cannat, M., Pablo Canales, J., Düsünür, D., Escartin, J., Miranda, J.M., 2006. Discovery of a magma chamber and faults beneath a Mid-Atlantic Ridge hydrothermal field. Nature 442, 1029–1032. https://doi.org/10.1038/nature05105.

Skolotnev, S.G., 2003. Gabbroids from the Vema Fracture Zone: textures, composition and tectonic setting. Petrology 11, 31–47.

Stolper, E., Walker, D., 1980. Melt density and the average composition of basalt. Contrib. Mineral. Petrol. 74, 7–12.

Streckeisen, A., 1973. Plutonic rocks. Classification and nomenclature recommended by the IUGS subcommission on the systematicsvof igneous rocks. Geotimes 18, 26–30.

Suhr, G., Johnson, K.T.M., Hellebrand, E., Brunelli, D., 2008. Stacked Gabbro units and intervening mantle: A detailed look at a section of IODP Leg 305, Hole U1309D. Geochem. Geophys. Geosyst. 9 (10), Q100007. https://doi.org/10.1029/2008GC002012.

Tollari, N., Toplis, M.J., Barnes, S.J., 2006. Predicting phosphate saturation in silicate magmas: an experimental study of the effects of melt composition and temperature. Geochim. Cosmochim. Acta 70, 1518–1536. https://doi.org/10.1016/j.gca.2005.11.024.

Toplis, M.J., Libourel, G., Carroll, M.R., 1994. The role of phosphorus in crystallisation processes of basalt: an experimental study. Geochim. Cosmochim. Acta 58, 797–810. https://doi.org/10.1016/0016-7037(94)90506-1.

Van Andel, T.H., Von Herzen, R.P., Phillips, J.D., 1971. The Vema Fracture Zone and the tectonics of transverse shear zones in oceanic crustal plates. Mar. Geophys. Res. 1, 261–283.

Watson, T.L., Taber, S., 1910. Nelsonite, a new rock type; its occurrence, association, and composition. Geol. Soc. Am. Bull. 21.

Wilcock, W.S.D., Hooft, E.E.E., Toomey, D.R., McGill, P.R., Barclay, A.H., Stakes, D.S., Ramirez, T.M., 2009. The role of magma injection in localizing black-smoker activity. Nat. Geosci. 2, 509.